Phosphorylation-Coupled Intramolecular Dynamics of Unstructured Regions in Chromatin Remodeler FACT

Manami Hashimoto,[†††△] Noriyuki Kodera,[¶△] Yasuo Tsunaka,[‡‡‡△] Masayuki Oda,[**] Mitsuru Tanimoto,[‖] Toshio Ando,[¶‖] Kosuke Morikawa,[‡§*] and Shin-ichi Tate[†††*]

[†]Department of Mathematical and Life Sciences, Hiroshima University, Hiroshima, Japan; [‡]Institute for Integrated Cell-Material Sciences (iCeMS), Kyoto University, Kyoto, Japan; [§]International Institute for Advances Studies, Kyoto, Japan; [¶]Bio-AFM Frontier Research Center, College of Science and Engineering, Kanazawa University, Kanazawa, Japan; [‖]School of Mathematics and Physics, College of Science and Engineering, Kanazawa University, Kanazawa, Japan; [**]Graduate School of Life and Environmental Sciences, Kyoto Prefectural University, Kyoto, Japan; [††]SENTAN, Japan Science and Technology Agency, Tokyo, Japan; and [‡‡]PRESTO, Japan Science and Technology Agency, Tokyo, Japan

ABSTRACT The intrinsically disordered region (IDR) of a protein is an important topic in molecular biology. The functional significance of IDRs typically involves gene-regulation processes and is closely related to posttranslational modifications such as phosphorylation. We previously reported that the *Drosophila* facilitates chromatin transcription (FACT) protein involved in chromatin remodeling contains an acidic ID fragment (AID) whose phosphorylation modulates FACT binding to nucleosomes. Here, we performed dynamic atomic force microscopy and NMR analyses to clarify how the densely phosphorylated AID masks the DNA binding interface of the high-mobility-group domain (HMG). Dynamic atomic force microscopy of the nearly intact FACT revealed that a small globule temporally appears but quickly vanishes within each mobile tail-like image, corresponding to the HMG-containing IDR. The lifespan of the globule increases upon phosphorylation. NMR analysis indicated that phosphorylation induces no ordered structure but increases the number of binding sites in AID to HMG with an adjacent basic segment, thereby retaining the robust electrostatic intramolecular interaction within FACT even in the presence of DNA. These data lead to the conclusion that the inhibitory effect of nucleosome binding is ascribed to the increase in the probability of encounter between HMG and the phosphorylated IDR.

INTRODUCTION

In recent years data derived from bioinformatics, protein physical chemistry, and tertiary structure analyses, such as x-ray crystallography and NMR, have led to the conclusion that numerous functional proteins contain regions or domains that do not form well-defined orderly three-dimensional structures but rather exist as dynamic ensembles of interconverting flexible conformers (1–3). These intrinsically disordered regions (IDRs) are ubiquitously found in eukaryotic proteins that play crucial roles in gene regulation within nuclei (4–8). It is known that these IDRs are involved in functionally important molecular recognition, where they fold into ordered conformations through binding to rigid ordered protein subunits or domains, a process that is generally termed coupled folding (9,10). Conversely, IDRs in a number of proteins do not necessarily undergo global disorder-to-order transitions upon binding. Moreover, several important regulatory interactions involve dynamic complexes in which main chains of IDRs continue to fluctuate without forming defined architectures (11,12). These binding events appear to be modulated by critical posttranslational modifications including phosphorylation, acetylation, methylation, and ubiquitination (8,11,13).

Our previous work reported that high-speed atomic force microscopy (HS-AFM) can simultaneously visualize each behavior of IDRs and rigid domains of *Drosophila* chromatin transcription-facilitating protein (dFACT) on a substrate surface in solution (14). This method is suitable for studying proteins involved in gene expression, such as transcriptional regulators and chromatin-remodeling factors. For example, FACT, classified as a chromatin remodeler, is a heterodimer complex that consists of SSRP1 and SPT16 subunits (Fig. 1). Both subunits contain several rigid domains and IDRs that play crucial roles in chromatin remodeling and transcriptional elongation (15–19). Thus, FACT is a suitable target for investigating the mechanistic and functional aspects of IDRs in solution through HS-AFM and NMR analyses.

In a previous study on interactions between dFACT and nucleosomes, we found that dFACT initially binds nucleosomes and/or nucleosomal DNA via a high-mobility-group domain (HMG) and an HMG-flanking basic ID segment (BID) of the dSSRP1 subunit, which jointly forms a DNA-binding element (Fig. 1) (20). The acidic ID segment (AID), adjacent to BID, forms intramolecular interactions with both HMG and BID (Fig. 1). Extensive phosphorylation of AID strikingly increases the number of negative charges, thereby strengthening the intramolecular interactions. As a result, the binding of dFACT to nucleosomal

Submitted October 10, 2012, and accepted for publication April 4, 2013.

△Manami Hashimoto, Noriyuki Kodera and Yasuo Tsunaka contributed equally to this work.

*Correspondence: tate@hiroshima-u.ac.jp or kmorikawa@icems.kyoto-u.ac.jp

Editor: Daniel Muller.

0006-3495/13/05/2222/13 $2.00

http://dx.doi.org/10.1016/j.bpj.2013.04.007

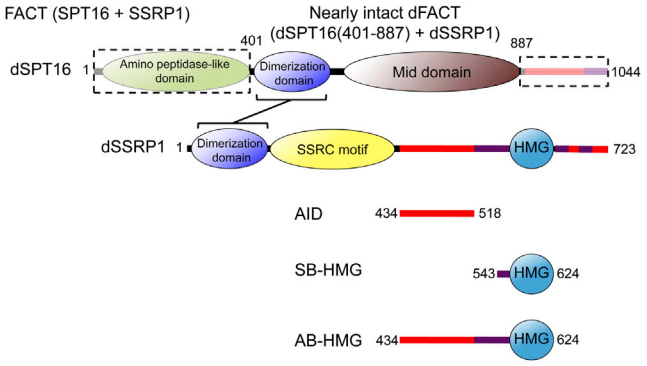

FIGURE 1 A schematic drawing of the domain organization of dSPT16 and dSSRP1, the two subunits in dFACT. The fragments used in this work are listed: AID; SB-HMG (residues 543–554), which contains a part of the BID region colored in purple (residues 519–554); and AB-HMG. These fragments jointly constitute the regulatory region of dSSRP1 binding to DNA. The heterodimeric complex, consisting of dSPT16 (residues 401–887) and the full-length dSSRP1, was used for HS-AFM measurements.

DNA is blocked, preventing the formation of rigid structures (20). The physiological significance of this control mechanism is highlighted by rapid chromatin transactions during early embryogenesis through dephosphorylation in the maternally transmitted dSSRP1 after fertilization (20). In humans, the dephosphorylated SSRP1, including the HMG, is essential for FACT to exhibit higher binding affinity with nucleosomes (19). In contrast, the yeast FACT-HMG functions as an isolated Nhp6a/b protein (15,21,22). Thus, the phosphorylation-dependent regulation is likely to be conserved only in higher eukaryotes. Despite the importance of AID phosphorylation, the detailed blocking mechanism remains unresolved at the atomic level.

To clarify the mechanism of intramolecular interaction between the AID segment and the DNA-binding elements, we investigated the detailed effects of phosphorylation by combining NMR spectroscopy and HS-AFM. Specifically, we prepared large amounts of various fragments, which were labeled with stable isotopes for NMR in both the phosphorylated and nonphosphorylated states, whereas FACT molecules nearly intact in size were observed by HS-AFM. Thus, this study allowed us to conclude that dense phosphorylation causes an electrostatic reinforcement of the interactions between the acidic ID region and the DNA-binding elements, and that the essence of the interactions is dynamic and transient, thus lacking specific and stable binding sites in domains or fragments.

MATERIALS AND METHODS

Protein preparation

The dFACT used was the same as that described in detail in our previous study (20). The fragments used in this work are schematically drawn in Fig. 1: AID, the short basic IDR plus HMG (SB-HMG), and the acidic and basic IDRs plus HMG (AB-HMG). These fragments were expressed in *Escherichia coli*. Details of the purification of each fragment and phosphorylation of the AID and AB-HMG fragments by casein kinase II (CK2) are described in the Supporting Material.

For the dynamic AFM experiments, the His-tagged *Drosophila* SPT16 (401–887) (dSPT16) and *Drosophila* SSRP1 (dSSRP1) were cloned into a pFastBacDual plasmid. To obtain the Ser/Thr-to-Ala mutants at the 10 phosphorylation sites (10SA; S443A, S472A, S476A, T477A, S488A, S496A, S500A, S502A, S506A, and S515A (Fig.S1 in the Supporting Material)), site-directed mutagenesis of the dFACT proteins was performed by the QuikChange method (Stratagene, La Jolla, CA). The nearly intact dFACT heterodimers (His-dSPT16 (401–887) + dSSRP1) were coexpressed as the fully phosphorylated form (wild–type (WT)) and a nonphosphorylated form (10SA) in Sf9 insect cells and purified as described previously (20).

Dynamic AFM analysis of the dFACT heterodimer

Dynamic AFM imaging experiments of the nearly intact dFACT heterodimers (Fig. 1) were carried out as described previously (14) using a laboratory-built HS-AFM (23,24). Briefly, we diluted the dFACT-WT or dFACT-10SA samples to ~2 nM with buffer A (20 mM Tris-HCl, pH7.5, 50 mM KCl, 10 mM $MgCl_2$, and 0.5% glycerol (vol/vol)). The diluted samples were used within 3 h. A droplet (2 μL) of a diluted sample was deposited on a freshly cleaved mica surface (~1 mm in diameter and <0.05 mm in thickness), which had been glued onto a glass stage (2 mm in diameter and 2 mm in height). After incubation for 3 min, molecules that were not attached to the mica surface were removed by rinsing with ~20 μL of buffer A. The sample surface was not allowed to dry. Subsequently, the sample stage was immersed in a liquid cell filled with ~60 μL of buffer A in which a small cantilever had been fixed. Imaging was carried out by HS-AFM in tapping mode. Details of the HS-AFM imaging experiments were summarized in a recent work (25). For image analysis, we applied three filters in the following order. First, a low-pass filter to remove spike noise; second, a flattening filter to make the *xy*-plane flat; third, a line-to-line base collection filter to minimize the base height difference between lines.

NMR spectroscopy

The backbone $^{1}H/^{13}C/^{15}N$ resonance assignments of AID and phosphorylated AID fragments were performed with a standard set of triple resonance experiments on a DMX600 spectrometer (Bruker, Billerica, MA). (BMRB entry 11511) Details are available in the Supporting Material.

NMR titration experiments

The interactions between the isolated AID and SB-HMG fragments were performed in two ways: one experiment used nonlabeled AID titrated into ^{15}N-labeled SB-HMG, and the other experiment involved titrating nonlabeled SB-HMG into ^{15}N-labeled AID. To explore how phosphorylation of AID influenced its interaction with binding partners, a phosphorylated AID fragment was also used in the titration experiments. The chemical-shift changes observed in a series of two-dimensional (2D) ^{1}H-^{15}N heteronuclear single-quantum coherence (HSQC) spectra during the titration were analyzed by numerical curve fitting to elucidate the number of effective binding sites, n, and the dissociation constants, K_D, according to a previously published procedure (26). In the calculations, we applied a global fitting procedure that incorporates all the chemical-shift-change profiles for the residues under study, with n and K_D as global adjustables (27). Monte Carlo simulation was applied to estimate the statistical errors for n and K_D, assuming an uncertainty for each peak position on a ^{1}H-^{15}N HSQC spectrum of 0.002 ppm (^{1}H) and 0.02 ppm (^{15}N), respectively, and using 64 synthetic data sets with Gaussian noise (28). Experimental details in the titration experiments between the isolated AID and SB-HMG fragments are described in the Supporting Material.

NMR analysis on the interaction between AB-HMG and double-stranded DNA

We carried out NMR spectral analysis for the ^{15}N-labeled nonphosphorylated and phosphorylated AB-HMG fragments in the absence and presence of DNA (Fig. 1). The limited solubility and the severe spectral overlap in the spectra of AB-HMG did not permit complete assignment of the resonances arising from the backbone nuclei. Only a limited number of resonances were assigned for AB-HMG. We used double-stranded DNA (dsDNA) with the sequence 5′-d(CGCGATATCGCG)$_2$-3′. The reaction mixture including the dsDNA was passed through a NAP-10 column to exchange the buffer to 50 mM Tris-HCl, pH 6.6, the buffer used for the NMR experiments.

RESULTS

Molecular features of phosphorylated and nonphosphorylated dFACT heterodimers visualized by HS-AFM

The wild-type dFACT (dFACT-WT) is spontaneously phosphorylated in Sf9 insect cells and is expressed as the fully phosphorylated form at 10 phosphorylation sites. In contrast, a dFACT mutant containing Ser/Thr-Ala substitutions at each of these sites, dFACT-10SA, is expressed as the nonphosphorylated form, as described previously (20). The molecular features of dFACT-WT (the phosphorylated form) and dFACT-10SA (the nonphosphorylated form) attached to mica surfaces in the buffer solution were directly visualized by HS-AFM (Fig. 2, *A* and *B*, respectively; also see Movies S1 and S2). At first glance, it appears that both molecules consist of a large globular domain and a long tail region. The large globular domain appears to be well adsorbed onto the mica surface, and its position does not change significantly over time. In contrast, the long tail region exhibits rapid fluctuations because of thermal agitations, indicating that this region has less affinity to the mica surface. These molecular features are consistent with the results of our previous study (14). Considering our previous data (14), we can assign the large globular domain (termed GD_1, see Fig. 2 *C*) to the structured domain consisting of dSPT16 (401−887) and dSSRP1 (1−404) (Fig. 1). The long tail region can be assigned to the IDR connected to the HMG (Fig. 1).

With careful observations, we noticed that the IDR has two small globular domains, which were connected with $IDR_{1–2}$ and $IDR_{2–3}$ (Fig. 2 *C*). One of the small globular domains (GD_3 (see Fig. 2 *C*)) was consistently observed at the end of the IDR and its appearance is not substantially different between the two constructs. In our previous study, this small globular domain was not observed, although the sample was prepared using the *E. coli* expression system. Furthermore, the amino acid sequence indicates no tertiary structure at the end of the IDR. Taken together, we postulate that unknown posttranslational modifications would induce a globular domain at the end of the IDR.

On the other hand, the other small globular domain (GD_2 (Fig. 2 *C*)) appears temporally around the middle of the IDR but shortly vanishes. In other words, we observed that the height of GD_2 changes over time. In addition, the figure of GD_2 appears to be retained for a longer period in dFACT-WT than in dFACT-10SA, whereas the length of the IDR appears to be slightly shorter in dFACT-WT than in dFACT-10SA. Notably, the distance between GD_1 and GD_2 appears to be much shorter in dFACT-WT; however, the distance between GD_2 and GD_3 is similar in both constructs. Similar tendencies were observed for most of the other protein molecules examined in each construct.

Quantitative analysis of distinct HS-AFM images between phosphorylated and nonphosphorylated dFACT

To quantitatively evaluate minute variations of the above-mentioned molecular features, we performed image analysis. Because the IDRs are highly flexible and can adopt similar molecular features at an arbitrary time, successive AFM images must be analyzed without skipping images to maintain arbitrariness of data sampling. To identify IDRs that contribute to changes in molecular features, a straightforward approach is required for contour length analysis of IDRs. However, considering the spatiotemporal resolution of the HS-AFM, it is currently not possible to apply contour-length analysis to successive AFM images without skipping images. As an alternative, we created a simple schematic representation of the molecular features of dFACT observed by HS-AFM (Fig. 2 *C*). In this schematic, the heights of the three globular domains (H_1–H_3) and the end-to-end distances between the two globular domains ($D_{1–2}$, $D_{2–3}$, and $D_{1–3}$) were obtained from a single AFM image. This approach allowed us to analyze almost all AFM images, even when the AFM images had poor signal/noise (S/N) ratios. The end-to-end distance can be used to adequately evaluate the length of a biological polymer on a surface, as described previously (29), and our data therefore support our interpretation. The analysis was performed on three typical molecules for the phosphorylated (dFACT-WT) and nonphosphorylated (dFACT-10SA) constructs, and the results are summarized in Table 1. We believe that the three molecules selected lie within the population as a whole of each construct, because most of the molecules observed displayed similar molecular features. For example, we can see four molecules of dFACT-10SA simultaneously (Movie S3), all of which appear to have similar molecular features. Note that the parameters described herein are not likely to have reached the most probable values, because we analyzed 4586–5770 images of only three molecules for each construct. However, we believe that these parameters will be convincing for our conclusions because they represent well the molecular features of each construct. The details are described below.

The distributions of H_1 appeared to be similar for both constructs, and the mean height was 3.9 nm (Fig. 3, *A*

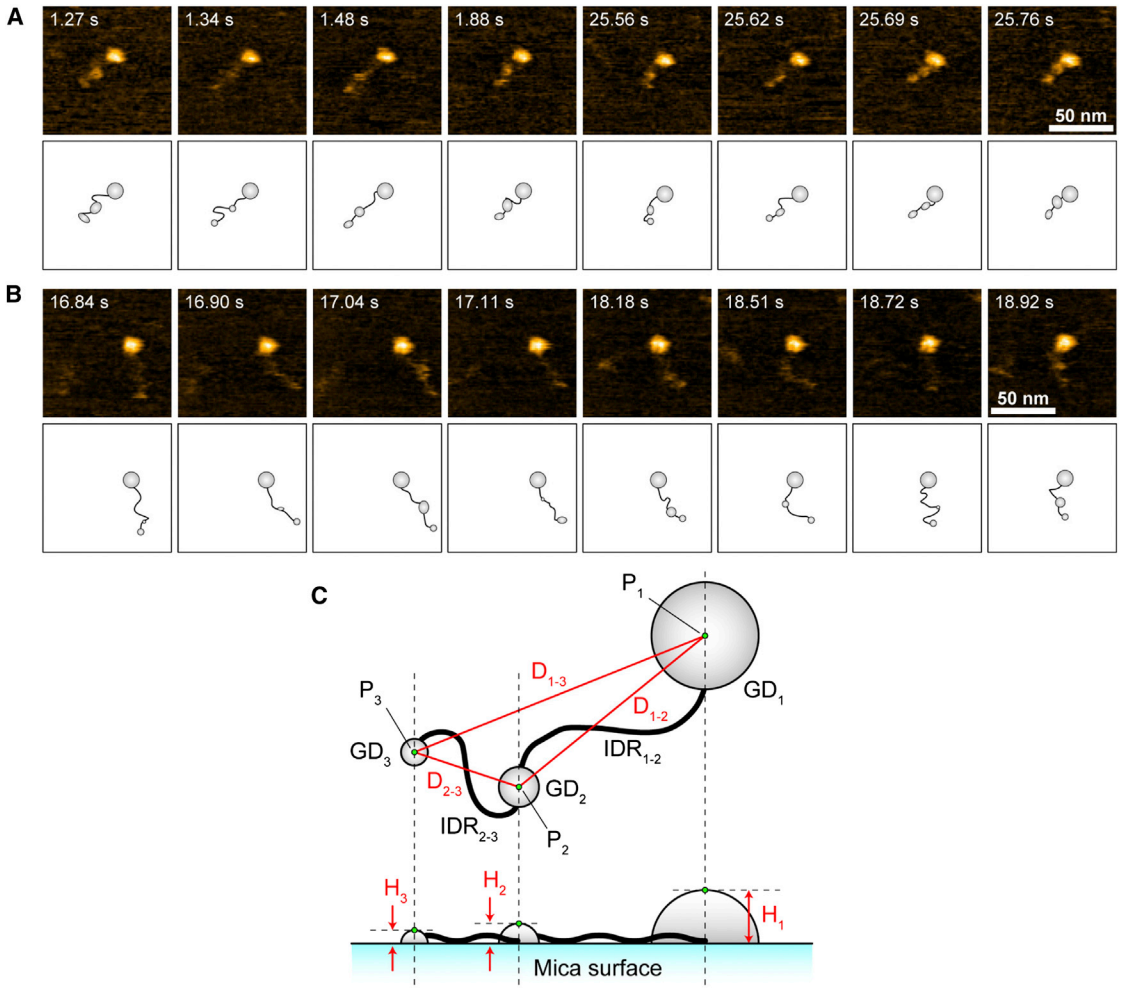

FIGURE 2 Typical HS-AFM images showing the molecular features of dFACT-WT (*A*) and dFACT-10SA (*B*). These HS-AFM images were clipped from the movie files (see Movie S1 for dFACT-WT and Movie S2 for dFACT-10SA). Every image was taken at 67.08 ms/frame (~15 frames/s). The time from the beginning of the clip is indicated at the upper left of each image. Scanning area, 100 × 100 nm^2 with 80 × 80 pixel; Z-scale, 4.0 nm. The observed molecular features of dFACT are schematized according to the definitions in *C*. These schematics were drawn freehand by tracing the AFM images by visual estimation. (*C*) Top-view (upper) and side-view (lower) schematics simply represent the characteristics of dFACT observed by HS-AFM. Gray-colored ellipses and black-colored thick solid lines represent the GDs and the IDRs, respectively. The symbols used for image analysis are also depicted. For every image, we selected three points (P_1–P_3) (*green dots*) representing the peak heights (H_i) in their respective GDs. Using these points, a distance from the highest point of one GD to that of another was determined. For example, the distance from P_1 of GD_1 to P_2 of GD_2 was expressed as $D_{1–2}$. In some images, the appearance of GD_2 or GD_3 was unclear; there was no point with distinct heights around the area usually seen. In this case, P_2 and P_3 with the highest height around the middle and the end of the IDR were selected.

and *D*, and Table 1), indicating no significant difference in the GD_1 for the two constructs. This height is the same as that obtained in our previous study (14). Although the distributions of H_3 appeared to differ, the mean height was 1.6 nm, with similar standard deviations for both constructs (Fig. 3, *C* and *F*, and Table 1), indicating that the GD_3 domain may not differ between the two constructs. In contrast, distributions for H_2 were notably higher for dFACT-WT than for dFACT-10SA (Fig. 3, *B* and *E*). Two peaks could be seen in the H_2 distribution of dFACT-10SA around 1.1 nm and 1.7 nm (Fig. 3 *E*). The peak around 1.1 nm was higher and wider than that around 1.7 nm, and the ratio of the areas of the two peaks was ~2:1 (low/high) (Fig. 3 *E*). Because we observed at least two physical states in GD_2 (i.e., a lower-height and a higher-height state), this result indicates that the GD_2 of dFACT-10SA tends toward a lower-height state than a higher one. On the other hand, the H_2 distribution of dFACT-WT appears to be a combination of a large peak around 1.6 nm and a small peak around 1.1 nm because a small shoulder around 1.1 nm could be seen in the distribution (Fig. 3 *B*). The area of the large peak was more than twice as wide as that of the small peak, indicating that the GD_2 of dFACT-WT tends toward a higher-height state than a lower one. Consequently, these results suggest that the GD_2 of dFACT-WT resides in the higher-height state much longer than does that of dFACT-10SA. Considering the two height values seen in the H_2 distributions (i.e., 1.1 nm for the lower-height state and

TABLE 1 Summary of the AFM image analysis

Parameter	dFACT-WT	dFACT-10SA
H_1	3.9 ± 0.3 nm	3.9 ± 0.3 nm
H_3	1.6 ± 0.3 nm	1.6 ± 0.4 nm
$D_{1–2}$	15 ± 5 nm	17 ± 5 nm
$D_{2–3}$	10 ± 3 nm	11 ± 4 nm
$D_{1–3}$	21 ± 5 nm	23 ± 7 nm
$D_{1–2}/(D_{1–2} + D_{2–3})$	0.59 ± 0.11	0.62 ± 0.11
Number of molecules analyzed	3	3
Number of frames analyzed	5770	4586

Heights and distances are shown by mean ± SD. Units of areas are arbitrary. The accuracy of the HS-AFM measurement for the *z*-direction (i.e., background noise) was 0.15 nm. The standard deviations of the Gaussian fits were therefore restricted to >0.15 nm. Note that we did not apply Gaussian fittings to the H_2 distributions because the results obtained had no statistical relevance.

1.6–1.7 nm for the higher-height state), the height of the HMG on one side corresponded to ~1 nm (30) and the height of the IDR was determined to be 0.4–0.6 nm. These data collectively suggest that the lower-height state (H_2 of ~1.1 nm) and higher-height state (H_2 of 1.6–1.7 nm) represent the HMG alone and the HMG associated with the IDR, respectively.

The distributions of $D_{2–3}$ were similar between dFACT-WT and dFACT-10SA (Fig. 3, *H* and *K*), and the mean length of $D_{2–3}$ showed almost the same values (Table 1). The length of $IDR_{2–3}$ did not change in response to phosphorylation. Meanwhile, the mean length of $D_{1–2}$ of dFACT-WT (15 ± 5 nm) was shorter by ~2 nm than that of dFACT-10SA (17 ± 5 nm) (Fig. 3, *G* and *J*, and Table 1). Therefore, the shorter state of $IDR_{1–2}$ within dFACT-WT (the phosphorylated form) is generated by the interaction between HMG and $IDR_{1–2}$, which contains the phosphorylated AID, but not that between HMG and $IDR_{2–3}$. The mean length of $D_{1–3}$ of dFACT-WT (21 ± 5 nm) was also shorter by ~2 nm than that of dFACT-10SA (23 ± 7 nm) (Fig. 3, *I* and *L*, Table1). This difference can be ascribed to the difference in the D_{1-2} for the two constructs because we observed no difference greater than 2 nm in D_{2-3}.

To estimate the mean position of the GD_2 in the long tail domain, the ratios of $D_{1–2}/(D_{1–2} + D_{2–3})$ for dFACT-WT (0.59 ± 0.11) and dFACT-10SA (0.62 ± 0.11) were determined (Fig. 4), indicating that phosphorylation of $IDR_{1–2}$ shifts the mean position of GD_2 to GD_1 but not to GD_3. Combined with the results in Fig. 3, these results demonstrate that the height change for GD_2 and the length changes for $D_{1–2}$ in dFACT-WT result from the interaction between the HMG and $IDR_{1–2}$, but not between the HMG and $IDR_{2–3}$. This observation is in good agreement with our previous model (20).

To summarize the HS-AFM data, GD_2 temporally appears and then vanishes in both constructs. However, it is important that the lifetime of the higher-height state in dFACT-WT is much longer than that in dFACT-10SA. In addition, dFACT-WT seems to have a shorter IDR than dFACT-10SA. These data indicate that the higher-height state of GD_2 originates from the interaction between the HMG and $IDR_{1–2}$, which contains the phosphorylated AID (Fig. 1). Analysis by HS-AFM is highly suitable for directly observing the dynamic behavior of large protein complexes on the surface of a substrate in solution. The findings described here should be analyzed by NMR, which can provide detailed local and atomic information on protein-protein interactions.

Structural characterization of the phosphorylated AID fragment

The fragments used in the NMR analysis are schematically drawn in Fig. 1. These fragments were expressed in *E. coli* and were phosphorylated by CK2 in vitro (Fig. S2). The limited signal dispersion of the isolated AID fragment in the 2D ^{1}H-^{15}N HSQC spectrum is typical of a disordered protein (Fig. 5 *A*). The $^{15}N\{^{1}H\}$ heteronuclear nuclear Overhauser effect (NOE) values for most residues of the AID were negative, indicating that the fragment is essentially in a disordered state. Residues around 453 showed positive heteronuclear NOE values. This region is rich in hydrophobic amino acids and is therefore likely to have restricted local backbone motions; although the motional properties do not seem functionally relevant (Fig. 5 *C*). CK2 successfully phosphorylated all nine canonical phosphoacceptor serines within the AID, as revealed from high-field NMR chemical shift changes in both the ^{1}H and ^{15}N dimensions (Fig. 5 *B*); T477 was not phosphorylated in this sample preparation, presumably due to the lower activity of CK2 toward Thr residues (31). The phosphorylation of AID did not induce any structural changes, because the increase in the resonance dispersion in the 2D ^{1}H-^{15}N HSQC spectrum (data not shown) was negligible. The $^{15}N\{^{1}H\}$ heteronuclear NOE profile for the phosphorylated AID (pAID) also indicated that it is in a disordered state (Fig. 5 *C*). Nonetheless, the heteronuclear NOE values of pAID did show an overall small but significant increase in the size of the NOE values when compared with the data for the nonphosphorylated form (Fig. 5 *C*). Presumably, electrostatic repulsion among phosphate groups may induce some fragment stiffness.

Interactions between the isolated AID and SB-HMG fragments

To elucidate the binding modes between isolated fragments, both the AID and pAID were titrated to the ^{15}N-labeled SB-HMG (Fig. 6, *A* and *B*), which contains a short basic IDR and the HMG (Fig. 1). The normalized chemical-shift changes observed in the 2D ^{1}H-^{15}N HSQC spectra of ^{15}N-labeled SB-HMG in the titration (Fig. 6, *A* and *B*) are plotted versus the residue numbers (Fig. 6, *C* and *D*). The comparison between the two profiles showed that AID and

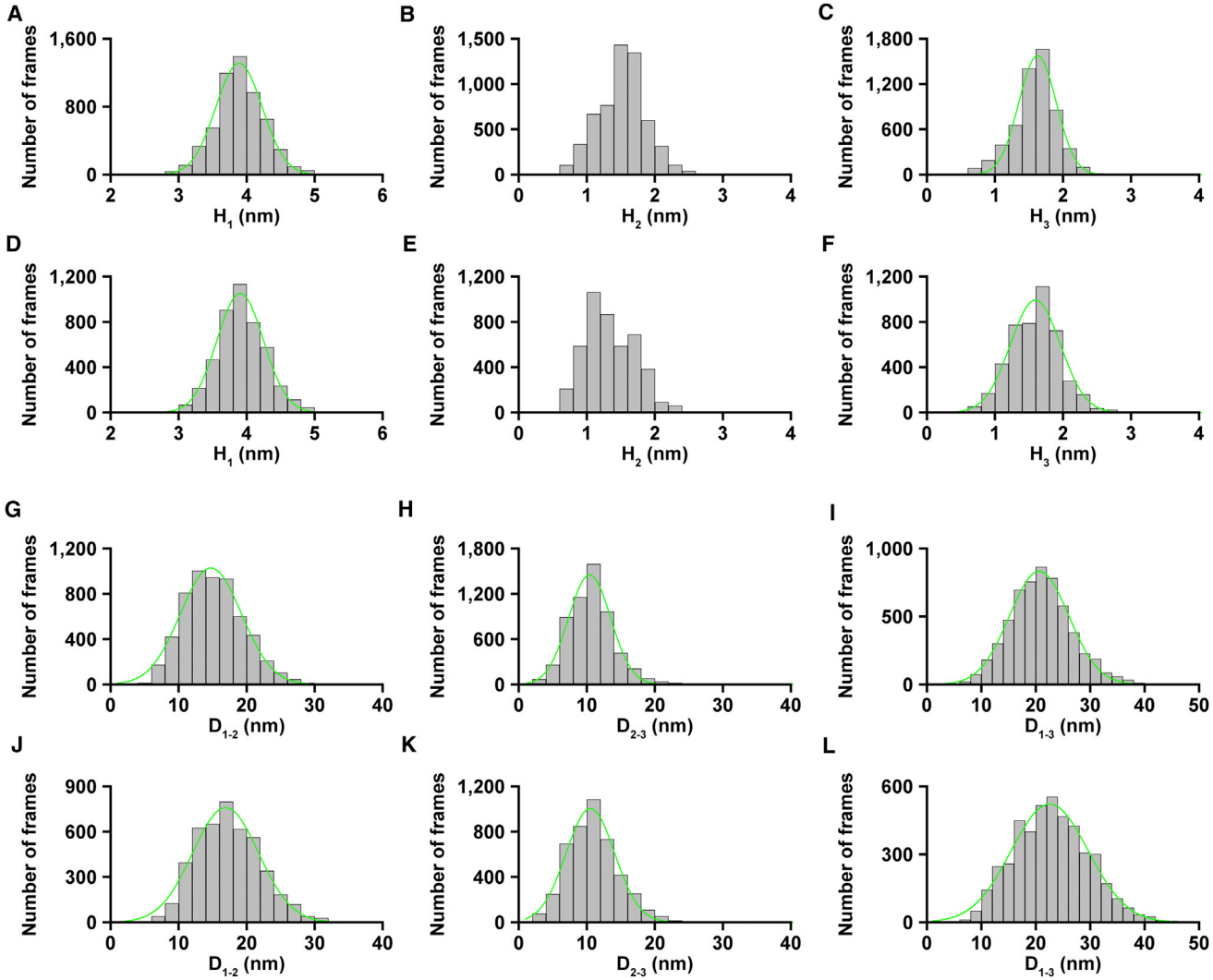

FIGURE 3 Height distributions of three GDs and distributions of distance between two GDs of dFACT. Height distributions (H_1–H_3) are shown for dFACT-WT (*A–C*) and dFACT-10SA (*D–F*). Distance distributions ($D_{1–2}$, $D_{2–3}$ and $D_{1–3}$) are shown for dFACT-WT (*G–I*) and dFACT-10SA (*J–L*). Green lines represent single-Gaussian fitting. Note that we did not apply Gaussian fittings to the H_2 distributions because the results obtained had no statistical relevance. A summary of the analysis is presented in Table 1. These results were obtained from analysis applied to three molecules for each construct.

pAID share similar binding sites on SB-HMG, irrespective of phosphorylation. Although they do have contact with the DNA binding surface of the HMG, both fragments primarily bind to the BID, because the residues in the BID showed greater chemical shifts than those in the HMG (Fig. 6, *C* and *D*). Furthermore, we found in our previous work that the BID is essential for intramolecular interaction with the AID (20). The magnitudes of the chemical shift changes by the addition of pAID are overall greater than those observed for AID binding, indicating that pAID is likely to have higher affinity to SB-HMG. That is, the increase in the population of the bound form of SB-HMG with pAID causes greater spectral changes relative to the free-state spectrum (27).

The numerical fittings to the chemical shift changes against the molar ratios of AID or pAID to SB-HMG showed that phosphorylation alters their binding modes to SB-HMG (Fig. 6, *E* and *F*) (26,32). To determine the K_D and n values from the experiments by using ^{15}N-labeled SB-HMG, we included in our calculation 11 residues for AID and 30 residues for pAID, showing that the significant changes deviated more than the mean + 1 SD (Fig. 6, *C* and *D*, *red bars*). The number of SB-HMG-binding sites on AID was estimated at $n = 2.0 \pm 0.1$ with a dissociation constant of $K_D = 9.7 \pm 0.3$ μM, assuming that all the binding sites on AID have equivalent affinities for SB-HMG. In the case of SB-HMG binding to pAID, the number of binding sites was estimated at $n = 3.9 \pm 0.1$ with $K_D = 1.01 \pm 0.02$ μM. This indicates that phosphorylation of AID doubles its number of SB-HMG-binding sites in addition to enhancing its affinity for SB-HMG. In agreement with these data from NMR, isothermal calorimetry (ITC) experiments

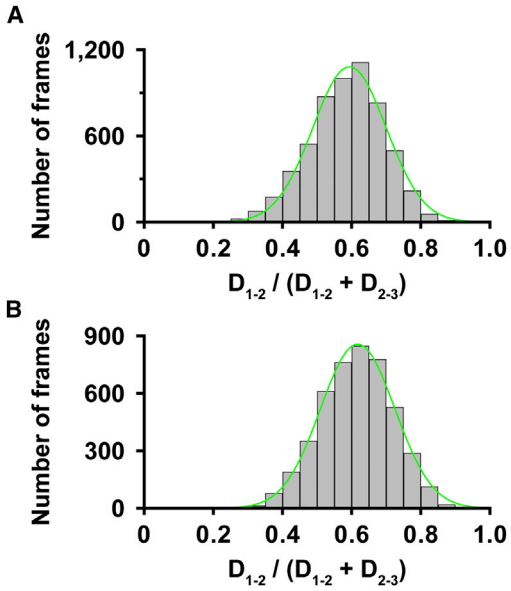

FIGURE 4 Plots showing the ratio of $D_{1-2}/(D_{1-2} + D_{2-3})$, which indicate the mean positions of GD_2 in the tail regions of dFACT-WT (*A*) and dFACT-10SA (*B*). Green lines represent single-Gaussian fitting. A summary of the analysis is presented in Table 1. These results were obtained from analysis applied to three molecules for each construct.

using the SB-HMG and AID or pAID showed that the number of binding sites on AID approximately doubles, depending upon phosphorylation (data not shown).

The SB-HMG titration to ^{15}N-labeled AID or pAID was also examined. The spectral changes in the 2D ^{1}H-^{15}N HSQC spectra for AID and pAID are shown in Fig. 7, *A* and *B*, respectively. The 20 residues in AID showed significant spectral changes (chemical-shift changes deviating by more than the mean + 1 SD of the entire data) upon binding to SB-HMG. It is thus likely that these residues are involved in binding to SB-HMG (Fig. 7 *E*). The residues are classified into two groups according to their affinity (nine high-affinity residues (Fig. 7 *C*, *left*, and Fig. 7 *E*, *blue bars*) and 11 low-affinity residues (Fig. 7 *C*, *right*, and Fig. 7 *E*, *red bars*)). The global fitting calculation, using the chemical shift profiles for the nine high-affinity residues gave a K_D value of 3.7 ± 0.1 μM, whereas the K_D value for the 11 low-affinity residues was 43 ± 1 μM. It should be noted that one-to-one binding was assumed in these calculations. The residues showed linear spectral changes according to SB-HMG concentration (Fig. 7 *A*), indicating that the high- and low-affinity residues do not form individual binding sites. If residues with different affinities form individual binding sites, the chemical-shift-change profiles should become nonunidirectional (33). Therefore, the binding surfaces on AID for SB-HMG may contain both high- and low-affinity residues. In fact, the residues of ^{15}N-labeled SB-HMG (Fig. 6 *C*, *red bars*) showed a slightly lower affinity for AID ($K_D = 9.7 \pm 0.3$ μM) than did the high-affinity residues in AID ($K_D = 3.7 \pm 0.1$ μM). These results imply that the high- and low-affinity residues of AID do not interact with SB-HMG in an individual manner but form multiple complexes in a dynamic equilibrium (i.e., a dynamic complex) (34).

The titration experiments using ^{15}N-labled pAID showed that pAID could accommodate up to four SB-HMG molecules (Fig. 7, *B* and *D*), which is consistent with the result from the analysis using ^{15}N-labeled SB-HMG ($n = 3.9 \pm 0.1$). Some residues in pAID showed nonunidirectional spectral changes in the titration of SB-HMG (Fig. 7 *B*). These residues are localized in the C-terminal half, which is rich in phosphoserine and acidic residues (Fig. 7 *F*, *green bars*). Similar to the nonlinear spectral changes in multiple ligands binding to the protein (27,35), it is likely that multiple SB-HMGs bind to the phosphor-Ser-rich region of pAID. The nonunidirectional spectral changes may therefore be caused by the expansion of the phosphor-Ser-rich region in response to the multiple bindings of SB-HMG.

Taken together, these data allowed us to conclude that nonphosphorylated AID contains binding surfaces that can accommodate up to two SB-HMG molecules, whereas phosphorylation of AID expands the surface by a factor of 2. The binding surfaces expanded by phosphorylation should increase the intramolecular encounter probability between the AID and BID-HMG segments in the dSSRP1 subunit.

Changes of intramolecular interactions between AID and BID-HMG in response to phosphorylation and dsDNA binding

To explore how AID forms intramolecular interactions with BID-HMG, we compared the 2D ^{1}H-^{15}N HSQC spectra of an AB-HMG fragment and the isolated AID (Fig. S3). The limited solubility (<0.1 mM) and the longer IDR of AB-HMG hampered assignment of the resonances of the backbone nuclei. Only a limited number of signals for rather isolated Ser residues were assigned based on the close proximity (i.e., similar chemical shifts) of the resonances for the AB-HMG construct to those assigned in the spectra of isolated AID or SB-HMG fragments (Fig. S3).

The significant spectral differences between AB-HMG and the isolated AID demonstrated that part of the AID segment binds to the other part of the AB-HMG intramolecularly (Fig. S3 *A*). The spectral difference between the two fragments remained in the presence of double-stranded DNA (dsDNA) (Fig. S3 *B*). This observation shows that the AID segment in the AB-HMG fragment still contacts other parts of the fragment without being released to behave as an isolated fragment, which would give NMR signals that match more closely to those for the isolated AID fragment.

The spectral difference between the pAB-HMG and the isolated pAID was apparent, indicating that the pAID segment in the pAB-HMG fragment has intramolecular contacts with other parts of the fragment (Fig. S3 *C*). The presence of the dsDNA did not completely reverse the spectral difference (Fig. S3 *D*), indicating that it does not block

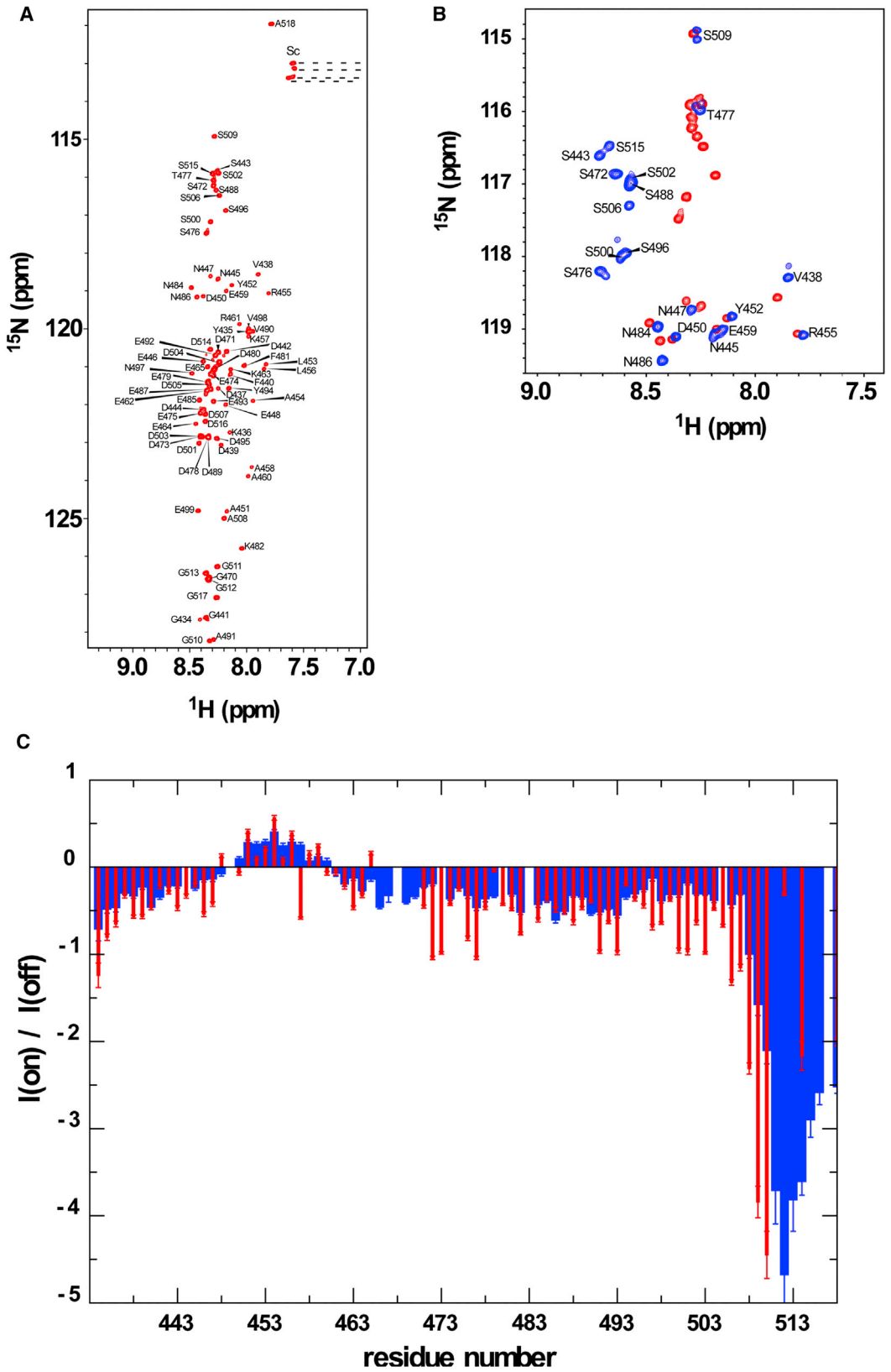

FIGURE 5 NMR spectral characterization of AID fragments. (*A*) Backbone resonance assignments of ^{15}N-labeled AID in the 2D ^{1}H-^{15}N HSQC spectrum. (*B*) Spectral comparison in a region of the 2D ^{1}H-^{15}N HSQC spectra for nonphosphorylated (*red*) and phosphorylated AID (*blue*). The backbone amide signals of the phosphorylated Ser shows an upfield shift in both the ^{1}H and ^{15}N dimensions. (*C*) Comparison of the ^{15}N{^{1}H} heteronuclear NOE profiles between nonphosphorylated (*red*) and phosphorylated (*blue*) AID fragments.

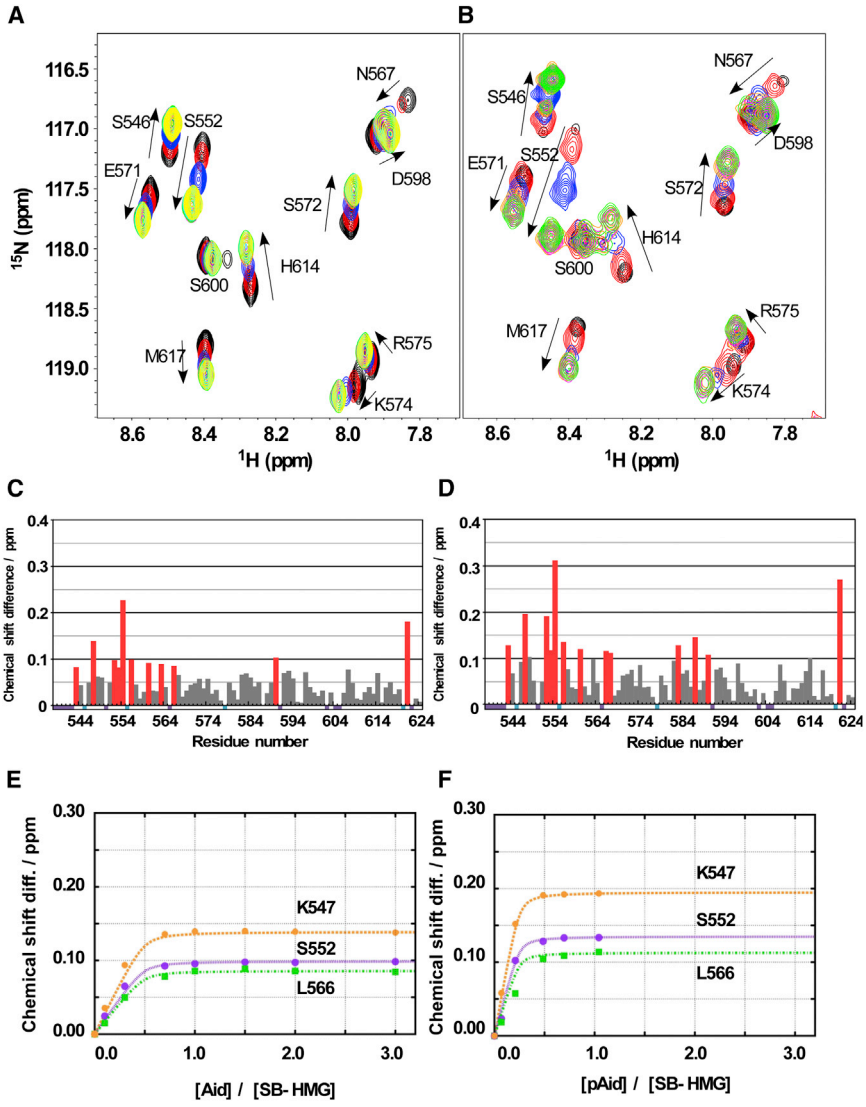

FIGURE 6 NMR titration experiments using the ^{15}N-labeled SB-HMG fragment. (*A*) Chemical-shift changes in the titration of nonphosphorylated AID fragment (AID) to ^{15}N-labeled SB-HMG; AID/SB-HMG molar ratios were 0.0 (*black*), 0.3 (*red*), 0.7 (*blue*), 1.0 (*orange*), 1.5 (*pink*), 2.0 (*green*), and 3.0 (*yellow*). (*B*) The corresponding spectral changes observed for phosphorylated AID (pAID); pAID/SB-HMG ratios were 0.00 (*black*), 0.07 (*red*), 0.21 (*blue*), 0.49 (*orange*), 0.70 (*pink*), and 1.04 (*green*). (*C* and *D*) Histograms of the chemical-shift differences in SB-HMG upon binding with AID (C) and pAID (*D*). Chemical-shift differences are plotted against residue numbers of SB-HMG. Red bars indicate that the chemical-shift differences are over the average plus one standard deviation. Short bars in cyan and purple along the *x* axis represent prolines and the residues for which assignment information was missing. Chemical-shift changes are shown for the representative residues in SB-HMG in the titrations with AID (*E*) and pAID (*F*). The numerically determined dissociation constant, $K_{D,}$ and number of binding sites, *n*, for the AID and pAID titration experiments were $K_D = 9.7 \pm 0.3\ \mu M$, $n = 2.0 \pm 0.1$ and $K_D = 1.01 \pm 0.02\ \mu M$, $n = 3.9 \pm 0.1$, respectively. Values for K_D and *n* were determined by global fitting using the residues marked by red bars in *C* and *D* (see Supporting Material).

the intramolecular contacts of the pAID segment with parts of the pAB-HMG fragment.

The absence of a complete set of resonance assignments for the AB-HMG and pAB-HMG fragments allows only a limited analysis of the intramolecular interactions between the AID and BID-HMG segments. Despite the experimental limits of this study, the spectral comparison shows that intramolecular interactions between the segments happen irrespective of phosphorylation, and that these interactions remain even in the presence of dsDNA; however, the modes of binding seem to change.

The intramolecular interactions were monitored using a limited number of assigned HMG signals (Fig. S4). In addition to the limited solubility of the AB-HMG fragment, intense signals from the long unstructured part in the AB-HMG prohibited observation of the signals from the HMG.

Despite the limited residues monitored, these NMR data collectively indicate that, irrespective of the phosphorylation state, the residues in HMG and BID retain contact with the AID segment, as suggested by the spectral difference in the HMGs in the AB-HMG and pAB-HMG fragments relative to the isolated HMG (Fig. S4). In the presence of dsDNA, the intramolecular contacts of HMG with the AID segment appear to change according to the phosphorylation state of the AID segment, as evinced by the spectral comparisons for residues A606, K621, and G553 (Fig. S4). The phosphorylation-dependent spectral changes for the HMG induced by the addition of dsDNA suggest that phosphorylation of the AID segment alters its interaction with the HMG box and thus changes the HMG-mediated binding to dsDNA.

DISCUSSION AND CONCLUSIONS

The combination of HS-AFM and NMR analyses has shown that phosphorylation of multiple serine residues in the AID

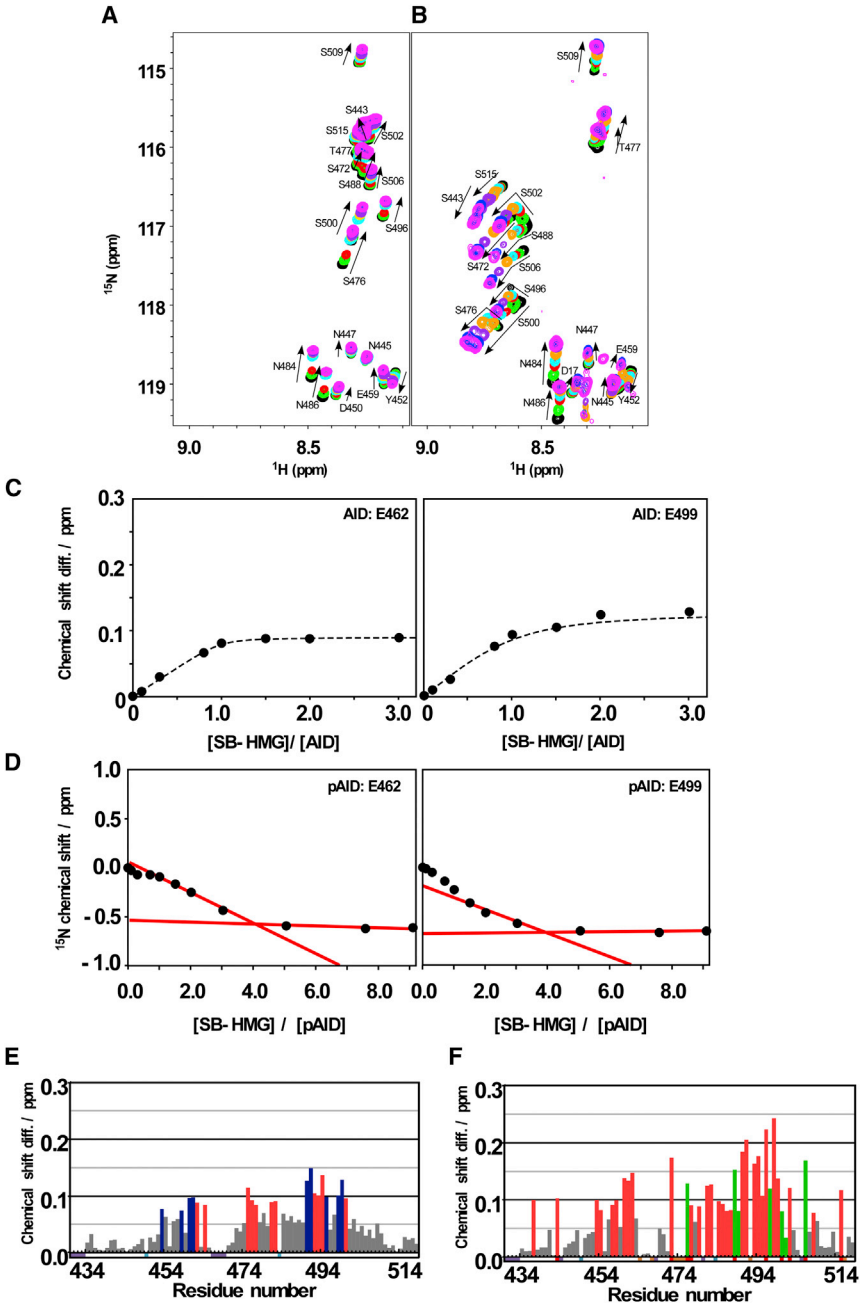

FIGURE 7 Spectral changes on ^{15}N-labeled AID and pAID in the titration with the unlabeled SB-HMG. (*A*) Spectral changes induced by the titration of AID; SB-HMG/AID ratios were 0.0 (*black*), 0.1 (*green*), 0.3 (*red*), 0.7 (*cyan*), 1.0 (*yellow*), 1.5 (*purple*), 2.0 (*blue*), and 3.0 (*pink*). (*B*) Spectral changes by pAID; SB-HMG/pAID ratios were 0.0 (*black*), 0.3 (*green*), 1.0 (*red*), 2.0 (*cyan*), 3.0 (*yellow*), 5.0 (*purple*), 7.0 (*blue*), and 9.0 (*pink*). (*C*) Chemical-shift-change profiles for representative residues in AID, showing the high (*left*) and low (*right*) affinities to SB-HMG. (*D*) The ^{15}N chemical-shift changes observed for representative residues in pAID according to the titration. Spectral changes determined that the maximal binding number of SB-HMG to pAID is 4. (*E* and *F*) Histograms of the chemical-shift differences in AID (*E*) and pAID (*F*) upon binding with SB-HMG. Chemical-shift differences are plotted against residue numbers for AID and pAID. Residues with a mean + 1 SD are colored. Residues in AID with blue bars have higher affinity (K_D = 3.7 ± 0.1 μM) than those with red bars (K_D = 43 ± 1 μM). The residues in pAID with green bars showed kinked titration traces, as in *B*. Short down bars in cyan and purple along the *x* axis indicate prolines and unassigned residues, respectively. Short down bars in red indicate phosphorylated Ser residues. Short down orange bars are residues whose signals were incompletely traced due to severe signal overlap during the titration.

modulates the intramolecular interactions between the AID and the DNA-binding element, which consists of BID and HMG. Our data collectively provide mechanistic insights into dynamic interactions between AID and the DNA-binding elements in FACT, as follows.

1. AID makes intramolecular contact with the DNA-binding elements. Phosphorylation of AID expands the binding epitope to the DNA-binding element by a factor of 2 when compared with the nonphosphorylated region.
2. The intramolecular contact of the nonphosphorylated AID with the DNA-binding element should be relatively weak, as demonstrated by the limited spectral changes in resonances from the isolated AID (Fig. S3). This is consistent with our HS-AFM observation that the nonphosphorylated FACT retains mostly extended IDRs (Fig. 3). Thus, the intramolecular contact between the nonphosphorylated AID and the DNA-binding element remains dynamic and transient.
3. Phosphorylation of AID reinforces its intramolecular interaction with the DNA-binding element, as shown by the larger spectral changes for the resonances representing the phosphorylated serines in the AID when compared with the same resonances in the isolated

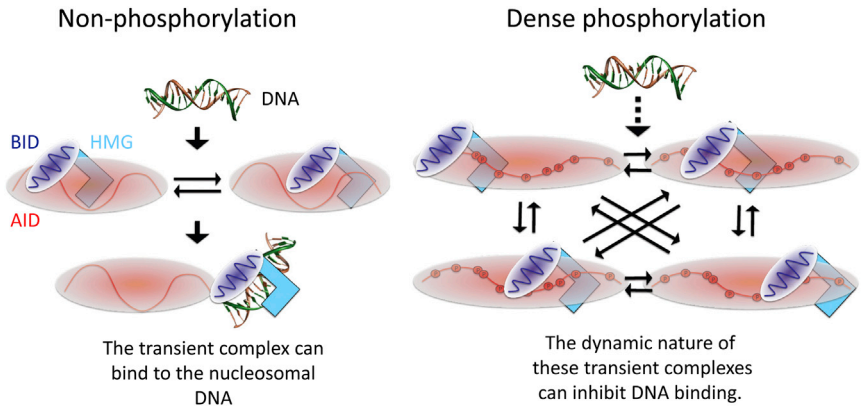

FIGURE 8 Summary of the mechanism underlying phosphorylation-dependent inhibition with respect to nucleosomal DNA. The intramolecular contact of nonphosphorylated AID with BID-HMG is nonspecific and dynamic. This situation allows BID-HMG to transiently bind with the nucleosomal DNA. In contrast, dense phosphorylation expands the AID region by elevating repulsive forces. This results in an increase of the probability of encounter between BID-HMG and pAID, thereby forming a more robust complex between BID-HMG and pAID. AID and BID are symbolically represented by the red and purple strings, respectively. Red and purple spheres indicate negative and positive net charges, respectively. The HMG is denoted by the cyan L-shaped structure. Red open circles labeled P indicate phosphorylation sites.

pAID (Fig. S3). The phosphorylated AID retained intramolecular contacts with the DNA-binding elements in the presence of DNA (Fig. S3), thus indicating that this AID element impairs FACT binding to DNA. In the presence of DNA, several resonances representing residues within the HMG showed chemical-shift changes, despite the fact that these residues retain contact with phosphorylated AID (Fig. S4). Our HS-AFM observation revealed dynamic behavior between folding and unfolding of the globular domain, which is putatively formed by pAID and BID-HMG (Fig. 3). Taken together, FACT involves dynamic and transient intramolecular interactions, even in the phosphorylated state.

The structure of the dSSRP1-HMG was similar to the yeast Nhp6a protein structure isolated from SSRP1 (30). The DNA-binding surface on the dSSRP1-HMG structure was similar to the DNA-binding surface in Nhp6A. The NMR structure of the Nhp6A-DNA complex revealed a characteristic L-shaped HMG fold, which contacts the minor groove of DNA, whereas an extended N-terminal BID region interacts with the adjacent major groove (36). The DNA-binding interface contains numerous conserved lysine and arginine residues that participate in electrostatic interactions with the phosphate backbone. Although some hydrophobic stacking/wedge interactions are formed between a number of Nhp6A residues and DNA bases, the interactions of Nhp6A with DNA are predominantly electrostatic. Our NMR data indicate that DNA and AID occupy almost the same electrostatic interaction interfaces on the HMG and BID regions regardless of the phosphorylation state of AID.

An apparently similar mechanism was proposed for the autoinhibition of DNA binding by phosphorylation of a transcription factor, Ets-1 (37,38). The affinity of Ets-1 to DNA is allosterically regulated by the flexibility of the unstructured serine-rich region and the inhibitory module, which is adjacent to the ETS domain responsible for DNA binding (38). Previous NMR experiments demonstrated that phosphorylation at several sites within the serine-rich region gradually shifts the equilibrium more to the rigid-inactive form, which is stabilized by stronger intramolecular interactions with both the inhibitory module and the DNA-binding domain (39). However, this inhibitory effect of Ets-1 is considerably different from our previous results, which showed no additive reduction of DNA-binding inhibition in response to the number of phosphorylated Ser/Thr mutations of dFACT (20). In the FACT mutant containing the SSRC motif, AID, BID, and HMG (Fig. 1), Ser/Thr-to-Ala mutations at two phosphorylation sites showed negligible inhibition of DNA binding, whereas mutations at four and six sites dramatically decreased the inhibitory effect (as shown in Fig. 3 *C* of Tsunaka et al. (20)). In other words, the inhibitory effect appears to be ultrasensitive, but not linear.

Our HS-AFM data provide, to our knowledge, a novel structural view, where the dynamic behavior of the FACT-IDR is drastically altered in response to phosphorylation. The NMR data showed that dense phosphorylation of the AID region increases binding sites with the DNA-binding elements containing the HMG. Presumably, the phosphorylation expands the AID region by elevating the repulsive forces, thus inducing a stronger interaction without protein folding. Moreover, the increase in binding sites caused by the phosphorylation of residues can be ascribed to a dynamic equilibrium among multiple binding states but not a simple two-state equilibrium, thereby blocking DNA binding (Fig. 8). This notion relates to the concept of encounter probability and differs to the mechanism observed for Ets-1.

This dynamic binding mode is rather similar to that in the electrostatic model proposed for the interaction between Cdc4 and Sic1 (34,40); the SCF ubiquitin ligase subunit Cdc4 interacts with the cyclin-dependent kinase inhibitor Sic1 in a dense phosphorylation-dependent manner (34). Multiple phosphorylation in the N-terminal IDRs of Sic1 leads to equilibrium engagement by an

interchange between phosphorylation sites (34). The degree of phosphorylation fine-tunes the complex formation of Sic1 with Cdc4 via long-range electrostatic interactions, ensuring ultrasensitivity of the Sic1-Cdc4 interaction caused by a net charge reversal (40). In agreement with this ultrasensitive change, our previous data showed that simultaneous mutations at four or six phosphorylation sites drastically enhance the binding ability of FACT to nucleosomal DNA (as shown in Fig. 3 *C* of Tsunaka et al. (20)). It is thus likely that the inhibitory mechanism of the phosphorylated FACT is essentially based on the electrostatic model.

Furthermore, a notable feature of this regulation mechanism is that the cooperative action of the tandemly linked AID and BID regions directs nucleosomal DNA binding through their interaction with the HMG in FACT. These tandemly linked IDRs may enhance the probability of encounter between the DNA-binding elements and the phosphorylated IDR in the inhibitory mechanism (Fig. 8). In fact, our HS-AFM analyses indicate that the lifetime of the globular domain in phosphorylated dFACT is much longer than that of the nonphosphorylated form.

Many atomic structures of protein complexes provide a general view that domain and/or subunit contacts take place on well-ordered surfaces that complement each other. However, functionally important complexes frequently involve dynamic, or transient, properties, which are derived from unstructured IDRs even upon complex formation. It is very likely that such flexibilities of protein complexes should change in response to posttranslational modifications, thereby regulating physiological functions. Thus, the combination of NMR and HS-AFM analysis used in this study potentially can be applied to many other protein complexes in which IDRs play important roles.

SUPPORTING MATERIAL

Four figures, three movies, supporting materials, and methods are available at http://www.biophysj.org/biophysj/supplemental/S0006-3495(13)00433-5.

This work was supported by Grants-in-Aid for Scientific Research on Innovative Areas (Research in a Proposed Research Area) (Ministry of Education, Culture, Sports, Science and Technology KAKENHI Grant No. 21113002, 21121006, and 23107724); a Grant-in-Aid for Japanese Society for the Promotion of Science Fellows (JSPS KAKENHI Grant No. 07J01196); the Mitsubishi Foundation; Japan Science and Technology (JST) Precursory Research for Embryonic Science and Technology; and JST Development of Systems and Technology for Advanced Measurement and Analysis.

REFERENCES

1. Dyson, H. J. 2011. Expanding the proteome: disordered and alternatively folded proteins. *Q. Rev. Biophys.* 44:467–518.
2. Uversky, V. N., and A. K. Dunker. 2010. Understanding protein nonfolding. *Biochim. Biophys. Acta.* 1804:1231–1264.
3. Uversky, V. N., and A. K. Dunker. 2012. Multiparametric analysis of intrinsically disordered proteins: looking at intrinsic disorder through compound eyes. *Anal. Chem.* 84:2096–2104.
4. Dyson, H. J., and P. E. Wright. 2005. Intrinsically unstructured proteins and their functions. *Nat. Rev. Mol. Cell Biol.* 6:197–208.
5. Garza, A. S., N. Ahmad, and R. Kumar. 2009. Role of intrinsically disordered protein regions/domains in transcriptional regulation. *Life Sci.* 84:189–193.
6. Uversky, V. N., C. J. Oldfield, and A. K. Dunker. 2008. Intrinsically disordered proteins in human diseases: introducing the D2 concept. *Annu. Rev. Biophys.* 37:215–246.
7. Uversky, V. N., C. J. Oldfield, …, A. K. Dunker. 2009. Unfoldomics of human diseases: linking protein intrinsic disorder with diseases. *BMC Genomics.* 10(*Suppl 1*):S7.
8. Vuzman, D., and Y. Levy. 2012. Intrinsically disordered regions as affinity tuners in protein-DNA interactions. *Mol. Biosyst.* 8:47–57.
9. Sugase, K., H. J. Dyson, and P. E. Wright. 2007. Mechanism of coupled folding and binding of an intrinsically disordered protein. *Nature.* 447:1021–1025.
10. Wright, P. E., and H. J. Dyson. 2009. Linking folding and binding. *Curr. Opin. Struct. Biol.* 19:31–38.
11. Fuxreiter, M. 2012. Fuzziness: linking regulation to protein dynamics. *Mol. Biosyst.* 8:168–177.
12. Mittag, T., L. E. Kay, and J. D. Forman-Kay. 2010. Protein dynamics and conformational disorder in molecular recognition. *J. Mol. Recognit.* 23:105–116.
13. Iakoucheva, L. M., P. Radivojac, …, A. K. Dunker. 2004. The importance of intrinsic disorder for protein phosphorylation. *Nucleic Acids Res.* 32:1037–1049.
14. Miyagi, A., Y. Tsunaka, …, T. Ando. 2008. Visualization of intrinsically disordered regions of proteins by high-speed atomic force microscopy. *ChemPhysChem.* 9:1859–1866.
15. Formosa, T. 2012. The role of FACT in making and breaking nucleosomes. *Biochim. Biophys. Acta.* 1819:247–255.
16. Nakayama, T., K. Nishioka, …, S. Hirose. 2007. *Drosophila* GAGA factor directs histone H3.3 replacement that prevents the heterochromatin spreading. *Genes Dev.* 21:552–561.
17. Reinberg, D., and R. J. Sims, 3rd. 2006. de FACTo nucleosome dynamics. *J. Biol. Chem.* 281:23297–23301.
18. Shimojima, T., M. Okada, …, S. Hirose. 2003. *Drosophila* FACT contributes to Hox gene expression through physical and functional interactions with GAGA factor. *Genes Dev.* 17:1605–1616.
19. Winkler, D. D., U. M. Muthurajan, …, K. Luger. 2011. Histone chaperone FACT coordinates nucleosome interaction through multiple synergistic binding events. *J. Biol. Chem.* 286:41883–41892.
20. Tsunaka, Y., J. Toga, …, K. Morikawa. 2009. Phosphorylated intrinsically disordered region of FACT masks its nucleosomal DNA binding elements. *J. Biol. Chem.* 284:24610–24621.
21. Brewster, N. K., G. C. Johnston, and R. A. Singer. 2001. A bipartite yeast SSRP1 analog comprised of Pob3 and Nhp6 proteins modulates transcription. *Mol. Cell. Biol.* 21:3491–3502.
22. Xin, H., S. Takahata, …, T. Formosa. 2009. yFACT induces global accessibility of nucleosomal DNA without H2A-H2B displacement. *Mol. Cell.* 35:365–376.
23. Ando, T., N. Kodera, …, A. Toda. 2001. A high-speed atomic force microscope for studying biological macromolecules. *Proc. Natl. Acad. Sci. USA.* 98:12468–12472.
24. Ando, T., T. Uchihashi, and T. Fukuma. 2008. High-speed atomic force microscopy for nano-visualization of dynamic biomolecular processes. *Prog. Surf. Sci.* 83:337–437.
25. Uchihashi, T., N. Kodera, and T. Ando. 2012. Guide to video recording of structure dynamics and dynamic processes of proteins by high-speed atomic force microscopy. *Nat. Protoc.* 7:1193–1206.
26. Yasuno, K., T. Yamazaki, …, Y. Kyogoku. 2001. Interaction of the C-terminal domain of the E. coli RNA polymerase α subunit with the

UP element: recognizing the backbone structure in the minor groove surface. *J. Mol. Biol.* 306:213–225.

27. Lian, L.-Y., and G. Roberts. 2011. Protein NMR Spectroscopy: Practial Techniques and Applications. Wiley, Chichester, United Kingdom.
28. Press, W. H., S. A. Teukolsky, …, B. P. Flannery. 1992. Numerical Recipes in C. Cambridge University Press, New York.
29. Rivetti, C., M. Guthold, and C. Bustamante. 1996. Scanning force microscopy of DNA deposited onto mica: equilibration versus kinetic trapping studied by statistical polymer chain analysis. *J. Mol. Biol.* 264:919–932.
30. Kasai, N., Y. Tsunaka, …, S. Tate. 2005. Solution structure of the HMG-box domain in the SSRP1 subunit of FACT. *J. Biomol. NMR.* 32:83–88.
31. Sarno, S., P. Vaglio, …, L. A. Pinna. 1996. Protein kinase CK2 mutants defective in substrate recognition. Purification and kinetic analysis. *J. Biol. Chem.* 271:10595–10601.
32. Fielding, L. 2007. NMR methods for the determination of protein–ligand dissociation constants. *Prog. Nucl. Magn. Reson. Spectrosc.* 51:219–242.
33. Arai, M., J. C. Ferreon, and P. E. Wright. 2012. Quantitative analysis of multisite protein-ligand interactions by NMR: binding of intrinsically disordered p53 transactivation subdomains with the TAZ2 domain of CBP. *J. Am. Chem. Soc.* 134:3792–3803.
34. Mittag, T., J. Marsh, …, J. D. Forman-Kay. 2010. Structure/function implications in a dynamic complex of the intrinsically disordered Sic1 with the Cdc4 subunit of an SCF ubiquitin ligase. *Structure.* 18:494–506.
35. Kleerekoper, Q., W. Liu, …, J. A. Putkey. 1998. Identification of binding sites for bepridil and trifluoperazine on cardiac troponin C. *J. Biol. Chem.* 273:8153–8160.
36. Murphy, E. C., V. B. Zhurkin, …, G. M. Clore. 2001. Structural basis for SRY-dependent 46-X,Y sex reversal: modulation of DNA bending by a naturally occurring point mutation. *J. Mol. Biol.* 312:481–499.
37. Hollenhorst, P. C., L. P. McIntosh, and B. J. Graves. 2011. Genomic and biochemical insights into the specificity of ETS transcription factors. *Annu. Rev. Biochem.* 80:437–471.
38. Pufall, M. A., G. M. Lee, …, B. J. Graves. 2005. Variable control of Ets-1 DNA binding by multiple phosphates in an unstructured region. *Science.* 309:142–145.
39. Lee, G. M., M. A. Pufall, …, L. P. McIntosh. 2008. The affinity of Ets-1 for DNA is modulated by phosphorylation through transient interactions of an unstructured region. *J. Mol. Biol.* 382:1014–1030.
40. Borg, M., T. Mittag, …, H. S. Chan. 2007. Polyelectrostatic interactions of disordered ligands suggest a physical basis for ultrasensitivity. *Proc. Natl. Acad. Sci. USA.* 104:9650–9655.

Supporting Materials

Phosphorylation-Coupled Intramolecular Dynamics of Unstructured Regions in Chromatin Remodeler FACT

Manami Hashimoto, Noriyuki Kodera, Yasuo Tsunaka, Masayuki Oda,
Mitsuru Tanimoto, Toshio Ando, Kosuke Morikawa, and Shin-ichi Tate

Supplementary Materials to MATERIALS AND METHODS

Preparation for the AID, SB-HMG and AB-HMG fragments

All of the dSSRP1 fragments (AID, SB-HMG and AB-HMG in Fig. 1A) were expressed and purified from *E.coli*. Each cDNA was cloned into pET28a (Novagen) and then transformed into BL21 (DE3) for the protein expression. These fragments were purified according to the following.

Cells were grown in the M9 medium with 0.05% ammonium chloride and 0.4% or 0.2% D-glucose as sole nitrogen and carbon source, respectively. The preparation for the isotopically labeled fragment used $^{15}NH_4Cl$ and/or ^{13}C-labled D-glucose. Protein expression was induced at the turbidity of the culture medium $OD_{600} = 0.6$ by adding IPTG to a final concentration of 0.5 mM. The cells harvested by centrifugation were resuspended by the buffer solution (50 mM Tris-HCl, pH 8.0) and subjected to sonication. The supernatant of the cell lysate was applied to HisTrap FF column (GE healthcare) to purify the His-tagged target fragment. The His-tag was cleared by thrombin at 4°C for 16 hours. The solution was further applied to HiTrap Q HP column (GE healthcare) or HiTrap Heparin HP column (GE Healthcare), for the AID and the HMG-containing fragments, respectively. A linear NaCl gradient from 0 to 1 M in the buffer solution (50 mM Tris-HCl, pH8.0) was applied to the column by using HPLC (Biologic DUOFLOW, Bio-Rad). The fractions containing the target fragment, monitored by UV absorbance at 280 nm, were collected and then dialyzed against the buffer solution (50 mM Tris-HCl, pH6.6) to remove NaCl. The dialyzed solution was concentrated with the concentrator device Amicon Ultra 3K (Millipore). The AID fragment was found to easily degrade during experiments, presumably due to a sparse amount of contaminated protease from cells. The purified AID fragment was, therefore, subjected to heat treatment (at 95°C for 5 min) to inactivate the unwanted proteases before concentration, thus keep the sample intact for a long experimental time, typically for a few weeks. This heat treatment to AID fragment did not cause any NMR spectral

changes on the ^{1}H-^{15}N HSQC spectra between the treated and the non-treated fragments.

Phosphorylation to the AID and AB-HMG fragments by CK2

The heat-treated AID fragment (0.05 mM) was incubated with 250 U CK2 (New England Biolabs) in 500 μl of reaction buffer containing 20 mM Tris-HCl, pH7.5, 50 mM KCl, 10 mM $MgCl_2$, 1 mM ATP (New England Biolabs) at 30°C for 40 hours. To gain the enough amount of the phosphorylated AID fragment subjected to the NMR experiments, typically 15 sets of the reaction mixtures were used. After the CK2 reaction, the solution was dialyzed against the buffer solution (50 mM Tris-HCl, pH6.6) and then concentrated, which solution was further applied to Zeba Desalt Spin Column (ThermoFisher) to remove the remaining ATP in the reaction mixture. The collected solution from the desalt spin column was finally dialyzed against the NMR sample buffer, 50 mM Tris-HCl, pH6.6. The extent of the phosphorylation was assessed by MALDI-TOFF MASS (AXIMA-CFR plus, SHIMAZU) (Fig. S1B). The phosphorylation to the AID fragment was also confirmed by SDS-PAGE stained with Pro-Q Diamond (Invitrogen) (Fig. S1A).

In the case of the phosphorylation to the AB-HMG fragment, the reaction condition was slightly changed from that applied to the AID fragment: the AB-HMG fragment in 0.05 mM concentration was treated with 500 U CK2 (New England Biolabs) with 1 mM ATP in the same reaction buffer at 30°C for 16 hours. The extent of the phosphorylation to the AB-HMG fragment was monitored with MALDI TOF-MASS (AXIMA-CFR plus, SHIMAZU), which showed all of the possible phosphorylation sites were modified (Fig. S1C). The state of the phosphorylation was also confirmed by NMR spectra, showing the substantial spectral changes for the phosphorylated residues on the ^{1}H-^{15}N HSQC spectra (Fig. 5). The phosphorylated AB-HMG fragment showed very limited solubility due to the intra- or possibly inter-molecular charge compensation, which prohibited the NMR signal assignments for the fragment.

NMR spectroscopy

The ^{15}N and $^{13}C/^{15}N$ labeled AID and SB-HMG fragments subjected to the present NMR analyses were purified from *E.coli* cell according to the purification procedures described above (AID fragment) and that in our previous work (SB-HMG). The proteins were dissolved in the buffer solution containing 50 mM Tris-HCl (pH 6.6). A set of triple resonance experiments, including HNCO, HNCA, HN(CA)CO, HN(CO)CA, CBCA(CO)NH, HNCACB, and HN(CA)NNH, was done to each fragment; AID,

phosphorylated AID and SB-HMG. The backbone resonance assignment of the SB-HMG was reported in our previous work, but the assignment was re-performed in the present sample condition, 50 mM Tris-HCl, pH 7.5, 50 mM KCl, 10 mM $MgCl_2$. All the triple resonance spectra were collected in a non-uniform sampling manner on a DMX600 spectrometer, 600 MHz for ^1H resonance frequency, at 293 K (20°C) for SB-HMG and 303 K (30°C) for AID. All data were processed with the Roland NMR toolkit. The ^1H-^{15}N HSQC spectra used in a series of titration experiments were collected in a normal sampling mode and processed with the program NMRPipe. The backbone assignment was done with the SPARKY software.

Steady state heteronuclear $^{15}N\{^1H\}$ nuclear Overhauser effect (NOE) measurements were carried out on a DMX600 at 303 K (30°C). ^1H saturation was done with a train of 270 degree-flip pulses for the duration of 2 sec with additional relaxation delay of 3 sec. For the reference spectra collected without ^1H saturation, 5 sec relaxation delay was applied. Each peak-intensity was estimated as the average peak heights of the nine points in a 3 by 3 grid centered at the peak position to alleviate spike noise effect, which was done by our home-written program. The error in reading each peak intensity was assumed to be the same as the root-mean-square (rms) noise calculated on the spectrum area having no signals by using the built-in suite in NMRPipe.

NMR titration experiments using AID and SB-HMG fragments

Two ways of NMR titration experiments were used; non-labeled AID is titrated into the ^{15}N-labeled SB-HMG, and the other is the *vice versa*. In the titration of non-labeled AID fragment into the ^{15}N-labeled SB-HMG, the SB-HMG concentration was adjusted to 0.3 mM, while AID was prepared to be 1.3 mM in concentration. Experiments were done at 293 K (20°C). An aliquot of the AID solution was put into the SB-HMG solution to achieve the following molar ratios: [AID]/[SB-HMG] = 0.0, 0.1, 0.3, 0.7, 1.0, 1.5, 2.0, and 3.0. Because of the limited concentration of the AID solution, significant volume of AID solution was put in each titration step, which caused non negligible dilution to SB-HMG. In the following titration curve analyses, this dilution effect was carefully considered to calculate the K_D value. In the case of the phosphorylated AID, pAID, titration into the ^{15}N-labeled SB-HMG, the AID fragment concentration was 0.9 mM and the following molar ratios were made: [pAID]/[SB-HMG] = 0.0, 0.1, 0.3, 0.7, 1.0, and 1.5. The titration curve was made in the same way as for the non-phosphorylated AID titration.

The titration of non-labeled SB-HMG (1.0 mM) into the ^{15}N-labeled AID (0.3 mM) was done in the following molar ratios: [SB-HMG]/[AID] = 0.0, 0.1, 0.3, 0.7, 1.0, 1.5, 2.0, 3.0. In the experiment to the ^{15}N-labeled phosphorylated AID, the data were collected in

the following molar ratios: [SB-HMG]/[pAID] = 0.0, 0.3, 1.0, 2.0, 3.0, 5.0, 7.0 and 9.0. All data were collected at 303 K (30°C). To reduce the spectral overlaps on the AID and pAID NMR data, the sample temperature was increased from that in the above titration experiment using ^{15}N-labeled SB-HMG.

In the titration curve analyses, the following function was used (1).

$$\Delta\delta = \frac{\Delta\delta_{sat}}{2[P]_t}\left\{(K_D + [P]_t + n[A]_t) - \left((K_D + [P]_t + n[A]_t)^2 - 4n[P]_t[A]_t\right)^{1/2}\right\} \quad \text{(Eq. 1)}$$

where, $\Delta\delta$ is the observed normalized chemical shift difference from the original position, which is defined as $\Delta\delta = \sqrt{\Delta\delta(^1\mathrm{H})^2 + (\Delta\delta(^{15}\mathrm{N})/5)^2}$; $\Delta\delta(^1\mathrm{H})$ and $\Delta\delta(^{15}\mathrm{N})$ are the chemical shift changes in ^{1}H dimension and ^{15}N dimension, respectively. $\Delta\delta_{sat}$ is the maximal chemical shift difference expected at the saturated binding. $[P]_t$ is the total concentration of the target protein, $[A]_t$ is the concentration of the titrated protein to be bound to the target protein and n is the possible binding sites on the target protein. K_D is the dissociation constant for the interaction between the target protein and the protein titrated.

In order to determine the K_D and n values from the experiments using ^{15}N-labeled SB-HMG, we applied a global fitting analysis, assuming that the K_D and n values were the same for all the residues selected (global parameters) (2). In the calculation, we used eleven residues for AID and 30 residues for pAID, which showed the significant changes deviated more than the average plus one standard deviation (Red bars in Fig. 6C and 6D). The errors for K_D and n were estimated by Monte Carlo simulation; the 64 synthetic datasets with Gaussian noises were used (3). The uncertainties for the peak positions on a ^{1}H-^{15}N HSQC spectrum, defining the magnitude of Gaussian noise in the synthetic data, were estimated at 0.002 ppm (^{1}H) and 0.02 ppm (^{15}N) from successively collected spectra.

In order to determine the K_D value from the experiment using ^{15}N-labeled AID, the function in Eq.1 with n fixed to one was used. In the first stage, K_D values for each residue were independently determined. According to individual K_D values, the residues were classified into two categories as high- and low-affinity residues; the former residues had K_D values in the order of 10^{-6} M and the other residues had K_D values in the order of 10^{-5} M. The K_D value for the nine high-affinity residues (blue bars in Fig. 7E) was determined by global fitting with K_D as a global parameter. In the other case, the eleven residues in the low-affinity class (red bars in Fig. 7E) were subjected to global fitting to obtain their K_D value. The error estimations for the K_D values were performed by a Monte Carlo simulation in the same manner as described above.

The global functional fitting to the observed titration data was done by our home-written program using the differential evolution method as an genetic algorithm (4).

Legend to Supplementary Figure

Fig.S1: The sequence of the AB-HMG fragment (residues 434–624). AID, BID and HMG are colored in red, purple and blue, corresponding to those in Figure 1. The potential phosphorylation sites by CK2 are marked in red boxes.

Fig. S2: Characterization of the phosphorylated AID and AB-HMG fragments. A. SDS-PAGE assays to monitor the phosphorylation to the AID fragments treated CK2: left, stained with coomasie brilliant blue; right, phosphorylated residue specific staining with Pro-Q Diamond (Invitrogen). B. The overlaid presentation of the MALDI-TOFF MASS data for the AID fragments treated with CK2 for 16 hours (blue), 24 hours (green), and 40 hours (yellow). The data in red is for the native AID fragment. C. The MALDI-TOFF MASS spectra for the native AB-HMG fragment and its phosphorylated form obtained through the 16-hour CK2 treatment.

Fig. S3: Spectral changes induced by DNA binding to AB-HMG and the phosphorylated AB-HMG (pAB-HMG). (A) The overlaid spectra for AB-HMG (red) and the isolated AID (black). (B) The spectra of AB-HMG in the presence of DNA (red) overlaid onto that of the isolated AID (black). (C) The overlaid spectra for pAB-HMG (red) and the isolated pAID (black). (D) The spectra of pAB-HMG in the presence of DNA (red) superimposed with that of the isolated pAID (black). Resonance assignments are marked to the particular signals of the isolated AID, pAID and AB-HMG.

Fig. S4: Spectral changes induced by DNA binding to the residues in HMG in the AB-HMG and the phosphorylated AB-HMG (pAB-HMG). Spectral changes of the particular residues within the isolated HMG (A, D, G), AB-HMG (B, E, H, J) and pAB-HMG (C, F, I, K) upon the addition of DNA. The spectra in the free (black) and DNA bound (red) states are superimposed. The isolated HMG does not contain G553 in the BID region.

Legends to Supplementary Movie

Movie S1: HS-AFM movie showing dFACT-WT on mica surface. Every image was taken at 67.08 ms/frame, and this movie is played at the rate of 15 frames/s. This movie consists of 500 images, and 8 images are picked up and shown in Fig. 2A. Scanning area, 100 × 100 nm^2 with 80 × 80 pixel; Z-scale, 4.0 nm.

Movie S2: HS-AFM movie showing dFACT-10SA on mica surface. Every image was taken at 67.08 ms/frame, and this movie is played at the rate of 15 frames/s. This movie consists of 500 images, and 8 images are picked up and shown in Fig. 2B. Scanning area, 100 × 100 nm^2 with 80 × 80 pixel; Z-scale, 4.0 nm.

Movie S3: HS-AFM movie showing dFACT-10SA on a mica surface. This movie shows four typical molecules of dFACT-10SA simultaneously, demonstrating that our samples are homogeneous. This movie was also observed on the mica surface. Every image was taken at 100.65 ms/frame, and this movie is played at the rate of 10 frames/s. This movie consists of 200 images. Scanning area, 200 × 200 nm^2 with 100 × 100 pixels; Z-scale, 4.0 nm.

REFERENCES

1. Yasuno, K., T. Yamazaki, Y. Tanaka, T. S. Kodama, A. Matsugami, M. Katahira, A. Ishihama, and Y. Kyogoku. 2001. Interaction of the C-terminal domain of the E. coli RNA polymerase α subunit with the UP element: recognizing the backbone structure in the minor groove surface. Journal of Molecular Biology 306:213-225.
2. Roberts, G. 2011. Structural and Dynamic Information on Ligand Binding. In Protein NMR Spectroscopy: Principal Techniques and Applications. L.-Y. Lian, and G. Roberts, editors.
3. Press, W. H., S. A. Teukolsky, W. T. Vetterling, and B. P. Flannery. 1992. Numerical Recipes in C. Cambridge University Press, New York.
4. Price, K., R. M. Storn, and J. A. Lampinen. 2005. Differential Evolutoin. Springer.

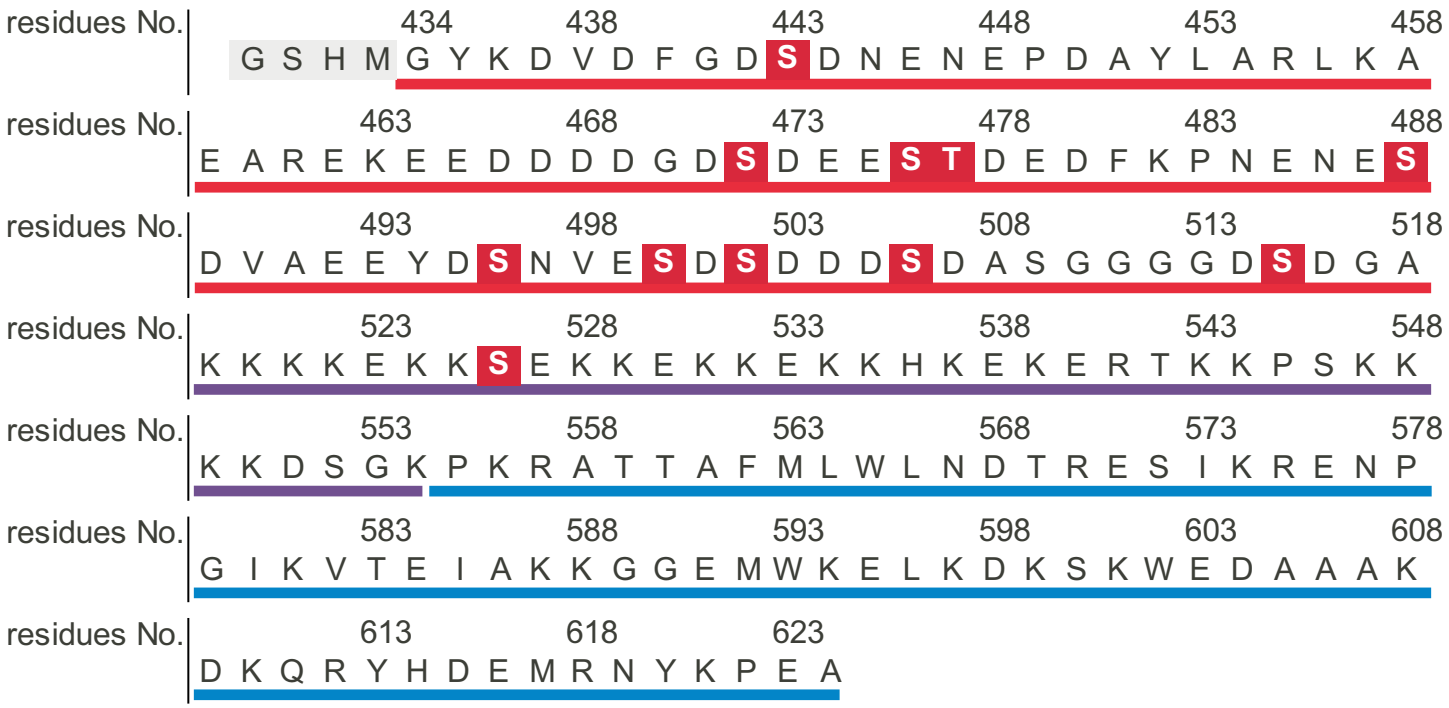
residues No.
434 438 443 448 453 458
G S H M G Y K D V D F G D S D N E N E P D A Y L A R L K A
residues No.
463 468 473 478 483 488
E A R E K E E D D D D G D S D E E S T D E D F K P N E N E S
residues No.
493 498 503 508 513 518
D V A E E Y D S N V E S D S D D D S D A S G G G G D S D G A
residues No.
523 528 533 538 543 548
K K K K E K K S E K K E K K E K K H K E K E R T K K P S K K
residues No.
553 558 563 568 573 578
K K D S G K P K R A T T A F M L W L N D T R E S I K R E N P
residues No.
583 588 593 598 603 608
G I K V T E I A K K G G E M W K E L K D K S K W E D A A A K
residues No.
613 618 623
D K Q R Y H D E M R N Y K P E A

Fig. S1

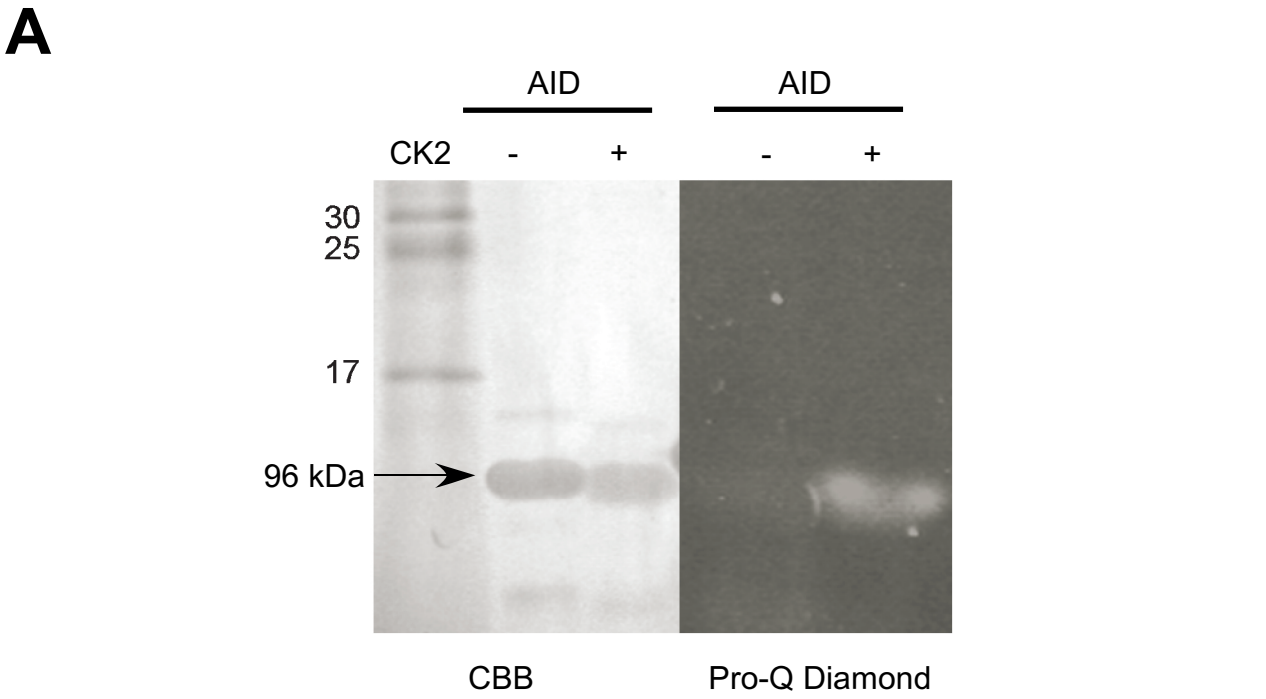
A
AID
AID
CK2
-
+
-
+
30
25
17
96 kDa
CBB
Pro-Q Diamond

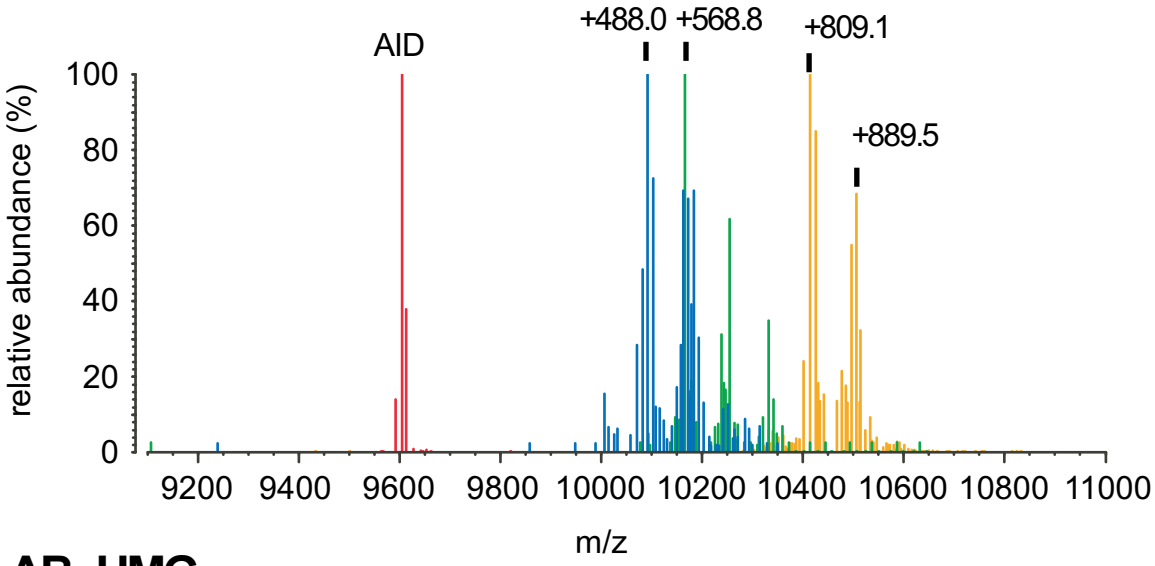
B AID
AID
+488.0
+568.8
+809.1
+889.5
relative abundance (%)
100
80
60
40
20
0
9200
9400
9600
9800
10000
10200
10400
10600
10800
11000
m/z

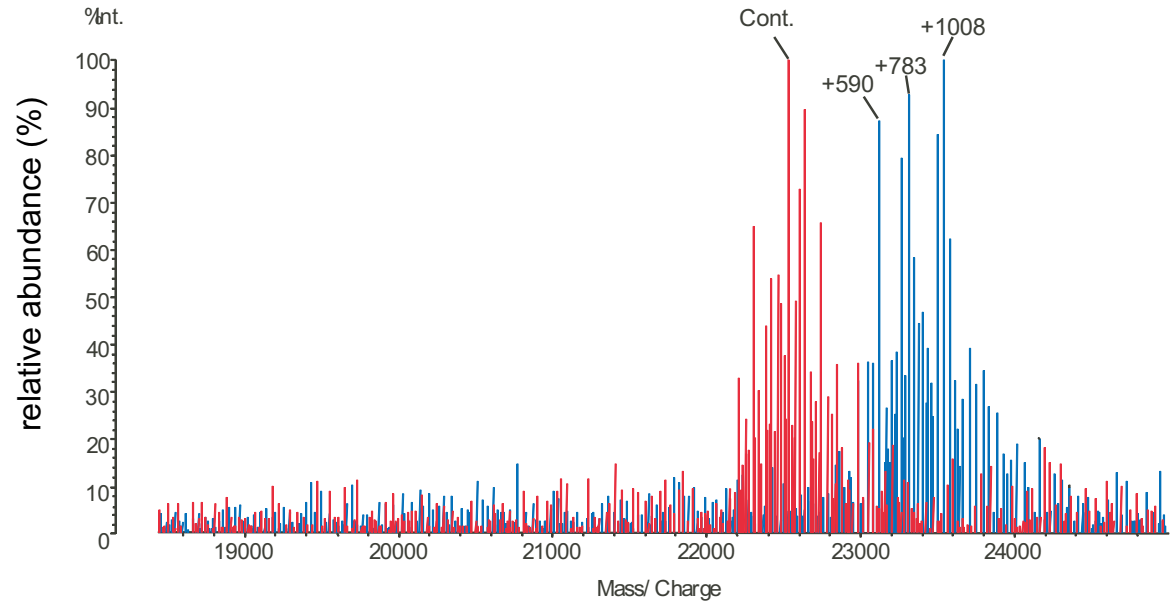
C AB- HMG
%Int.
Cont.
+1008
+783
+590
relative abundance (%)
100
90
80
70
60
50
40
30
20
10
0
19000
20000
21000
22000
23000
24000
Mass/ Charge

Fig. S2

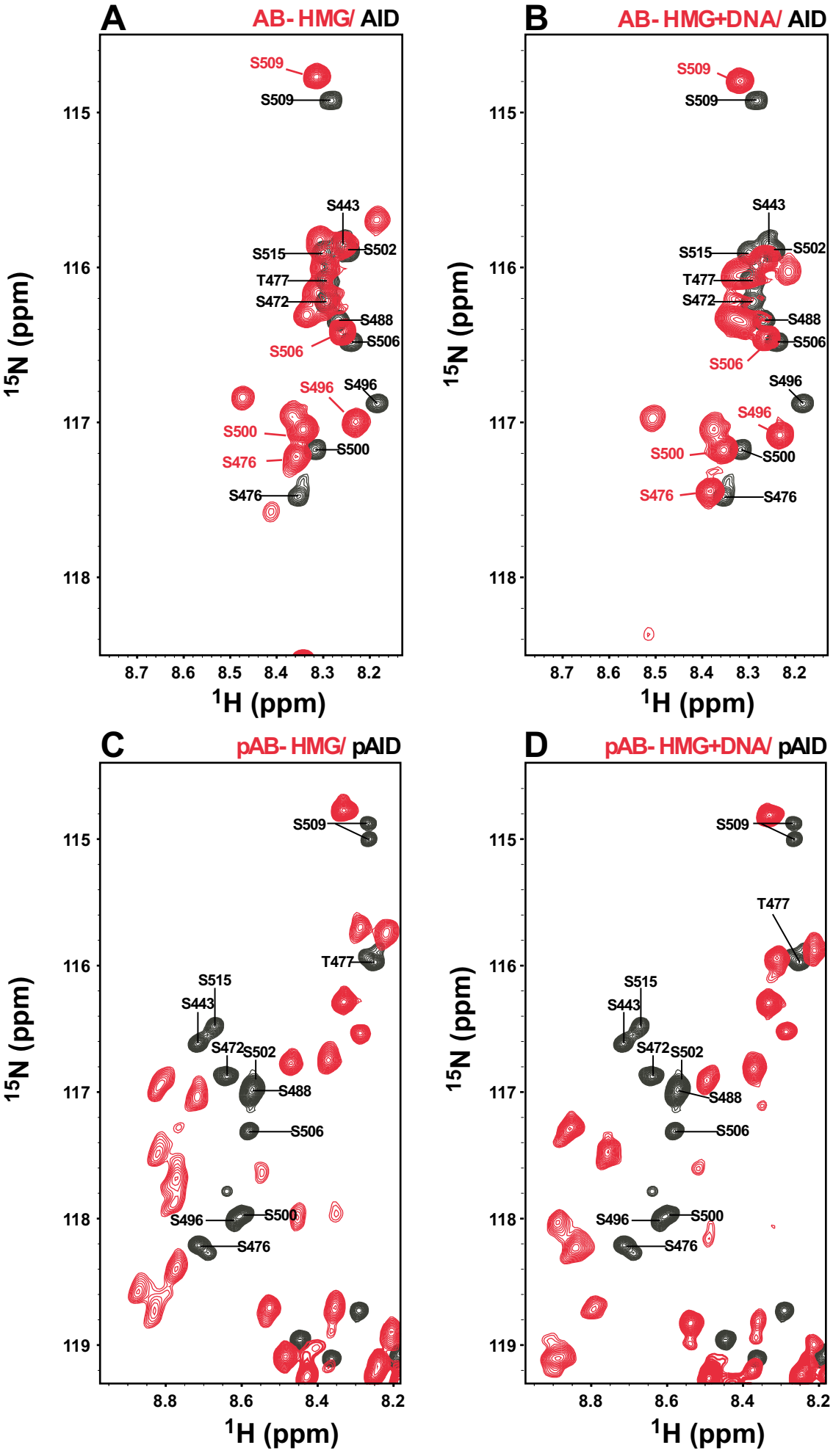
A
AB- HMG/ AID
B
AB- HMG+DNA/ AID
C
pAB- HMG/ pAID
D
pAB- HMG+DNA/ pAID
15N (ppm)
1H (ppm)
S509
S443
S515
S502
T477
S472
S488
S506
S496
S500
S476

Fig. S3

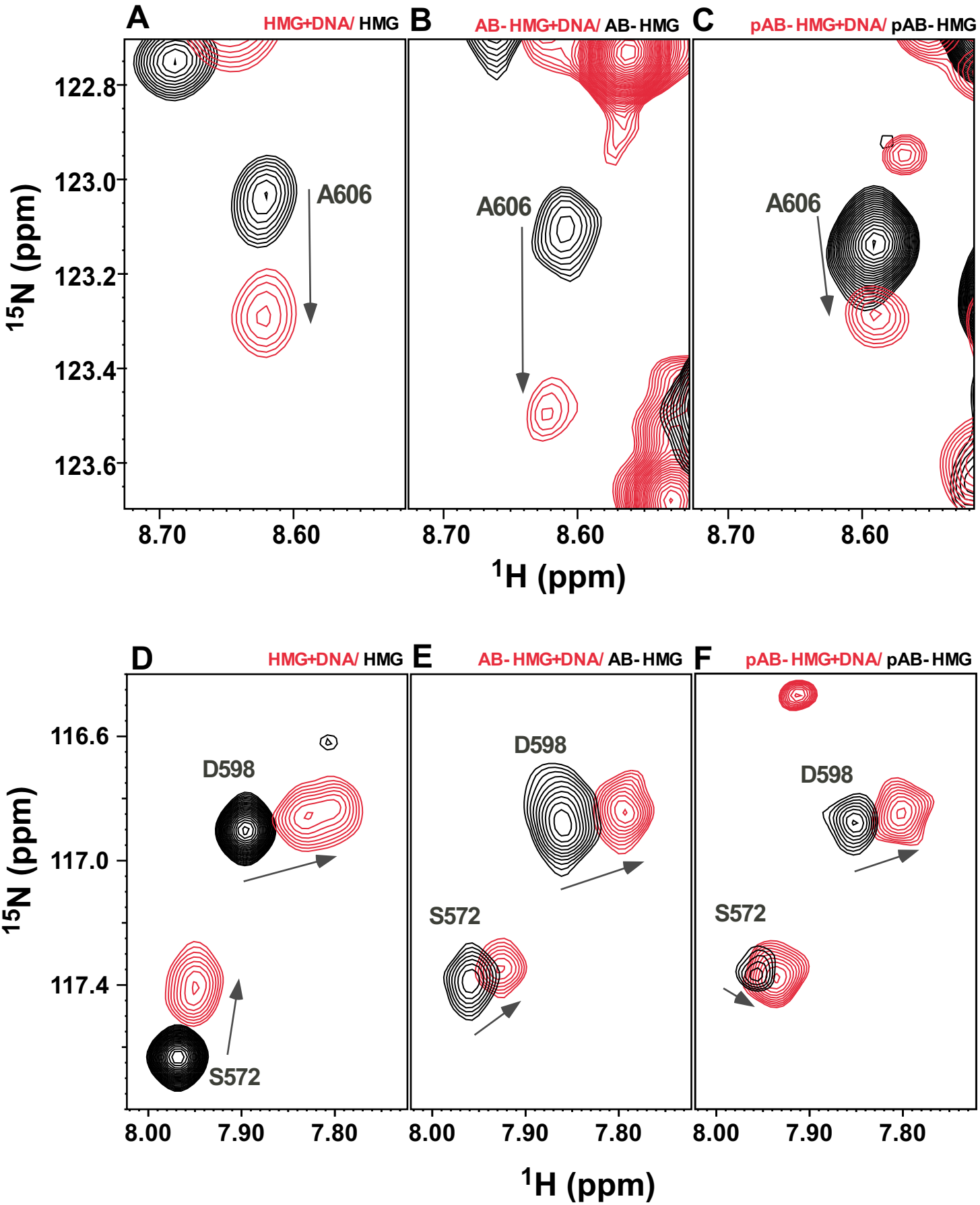
A
HMG+DNA/ HMG
B
AB-HMG+DNA/ AB-HMG
C
pAB-HMG+DNA/ pAB-HMG
A606
A606
A606
122.8
123.0
123.2
123.4
123.6
15N (ppm)
8.70
8.60
8.70
8.60
8.70
8.60
1H (ppm)
D
HMG+DNA/ HMG
E
AB-HMG+DNA/ AB-HMG
F
pAB-HMG+DNA/ pAB-HMG
D598
D598
D598
S572
S572
S572
116.6
117.0
117.4
15N (ppm)
8.00
7.90
7.80
8.00
7.90
7.80
8.00
7.90
7.80
1H (ppm)

Fig. S4-1

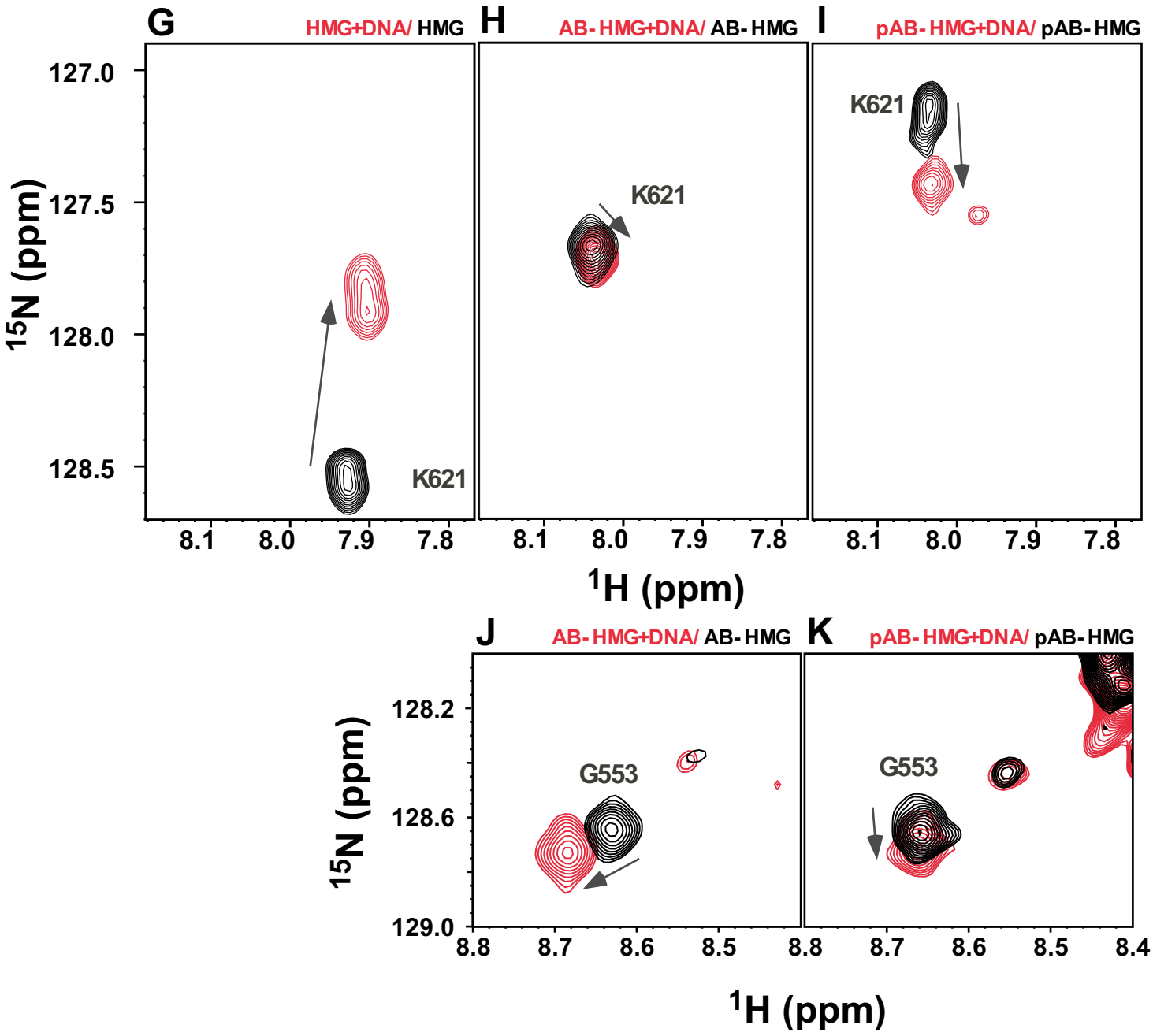
G
HMG+DNA/ HMG
H
AB-HMG+DNA/ AB-HMG
I
pAB-HMG+DNA/ pAB-HMG
K621
K621
K621
K621
127.0
127.5
128.0
128.5
15N (ppm)
8.1
8.0
7.9
7.8
1H (ppm)
J
AB-HMG+DNA/ AB-HMG
K
pAB-HMG+DNA/ pAB-HMG
G553
G553
128.2
128.6
129.0
15N (ppm)
8.8
8.7
8.6
8.5
8.4
1H (ppm)

Fig. S4-2